Cronfa - Swansea University Open Access Repository

_____

This is an author produced version of a paper published in:
Journal of Physics B: Atomic, Molecular and Optical Physics

_____

Cronfa URL for this paper:
http://cronfa.swan.ac.uk/Record/cronfa35078

_____

Paper:

Rasmussen, C., Madsen, N. & Robicheaux, F. (2017). Aspects of 1S-2S spectroscopy of trapped antihydrogen atoms. _Journal of Physics B: Atomic, Molecular and Optical Physics, 50_(18), 184002
http://dx.doi.org/10.1088/1361-6455/aa854c

_____

Aspects of 1S-2S spectroscopy of trapped antihydrogen atoms

C. Ø. Rasmussen

Aarhus University

N. Madsen

Swansea University

F. Robicheaux

Purdue University

(Dated: July 27, 2017)

Abstract

Antihydrogen atoms are now routinely trapped in small numbers. One of the purposes of this effort is to make precision comparisons of the 1S-2S transition in hydrogen and antihydrogen as a precision test of the CPT theorem. We investigate, through calculations and simulations, various methods by which the 1S-2S transition may be probed with only a few trapped atoms. We consider the known constraints from typical experimental geometries, detection methods, sample temperatures, laser light sources etc. and we identify a viable path towards a measurement of this transition at the 10^{-11} level in a realistic scenario. We also identify ways in which such a first measurement could be improved upon as a function of projected changes and improvements in antihydrogen synthesis and trapping. These calculations recently guided the first observation of the 1S-2S transition in trapped antihydrogen.

PACS numbers: 31.15.ac, 36.10.-k, 32.70.-n, 32.80.Fb

I.   INTRODUCTION

Antihydrogen ($\bar{\mathrm{H}}$), the bound state of an antiproton ($\bar{\mathrm{p}}$) and a positron (e^+), holds the promise of some of the most precise tests of fundamental symmetries between matter and antimatter such as e.g. the CPT theorem of particle physics. The CPT theorem states that the laws of physics remain unchanged under the combined operation of Charge conjugation, Parity inversion and Time reversal, e.g. the internal states of antihydrogen must be identical to those of hydrogen.

Hydrogen is one of the best measured systems in physics, the $1S$-$2S$ transition from the ground to the first excited state, holding the record of being measured to a precision of 4.2×10^{-15} [1]. This transition therefore holds the promise for the highest absolute precision comparison of hydrogen and antihydrogen. The prospect of which recently improved with the first observation of the $1S$-$2S$ transition in trapped antihydrogen by the ALPHA collaboration [2].

In this paper we will explore how to accomplish such a measurement on the antihydrogen atom within the context of current experimental efforts. There are a number of challenges to be faced to reach the precision of the measurement on hydrogen, the foremost being the very low number of available antihydrogen atoms and their relatively high temperature. Further complications stem primarily from the fact that the antihydrogen atoms must be made in the laboratory as they do not occur in Nature. This introduces a host of geometric constraints and is the root cause of the formerly mentioned issues. A key feature is that the number of $\bar{\mathrm{H}}$ is too low for beam type experiments like Ref. [1]. To obtain sufficient signal for a measurement, the interaction time of each atom with the laser is increased by confining them in a trap. This leads to new problems because neutral atom traps have strong magnetic fields that shift the energy levels and induce electric fields in the moving anti-atoms. The low number of $\bar{\mathrm{H}}$ (a maximum of $\sim$20 are trapped per experimental cycle [2]) furthermore means that detecting whether a transition has taken place is a challenge that can not be met with traditional methods used by measurements on normal atoms. Part of the work presented here underpinned the experimental choices made in the first observation of the $1S$-$2S$ transition in trapped antihydrogen [2].

II. ANTIHYDROGEN FORMATION AND TRAPPING

While part of this work will be of general interest to few-trapped-atom spectroscopy, our motivation and focus will be the particular issues related to antihydrogen as it is formed and trapped by the ALPHA collaboration [3]. Trapped antihydrogen was also reported by the ATRAP collaboration using very similar methods [4], and our discussion should also be directly applicable to that experiment. No other experiments are currently pursuing trapping or laser-spectroscopy of antihydrogen [5].

Antihydrogen is formed by merging cold plasmas of antiprotons and positrons. The charged particles in these experiments are held and manipulated in Penning-Malmberg traps. In a Penning-Malmberg trap charged particles are radially confined by a strong axial magnetic field and axially confined by electric fields from appropriate voltages applied to a number of co-axial cylindrical electrodes [6, 7]. The leptons are generally cooled through emission of cyclotron radiation, and they reach cryogenic temperatures as the traps are cooled to about 4 K. The antiprotons are sourced from the CERN AD at 5.3 MeV kinetic energy [8], trapped and prepared for mixing with the positrons as described in detail in Refs. [5, 9]. The latter reference also describes how the positrons sourced from a ^{22}Na radioactive source are prepared. The part of the ALPHA apparatus used for synthesising, trapping and investigating antihydrogen, shown in Figure 1, illustrates the typical geometry for antihydrogen experiments.

Once the antiprotons and positrons find themselves cooled in adjacent wells they can be brought to interact in various ways [5]. First though, the magnets that form the minimum-B trap for antihydrogen trapping are energised [10]. The minimum-B (antihydrogen) trap in ALPHA consists of, as a minimum, two co-axial short solenoids called mirror coils at each end of the axis of a 30 cm long octupole magnet, three additional short solenoids are spaced evenly between the two end coils to allow for e.g. flattening the axial field (Figure 1). Following the energisation of the antihydrogen trap, in ALPHA, the antiprotons and positrons are brought together by a slow ($\sim$1 s) potential manipulation [2]. For typically 9×10^4 antiprotons at $T_{\bar{p}} \approx 40$ K and radius $\sim$1.0 mm and 1.6×10^6 positrons at $T_{e+} \approx 20$ K and radius $\sim$0.7 mm, this results in the production of tens of thousands of antihydrogen atoms of which typically ten are trapped. The depth of the antihydrogen trap is about 50 μeV, or 0.5 K. Lasers may be introduced to the ALPHA system along four separate paths
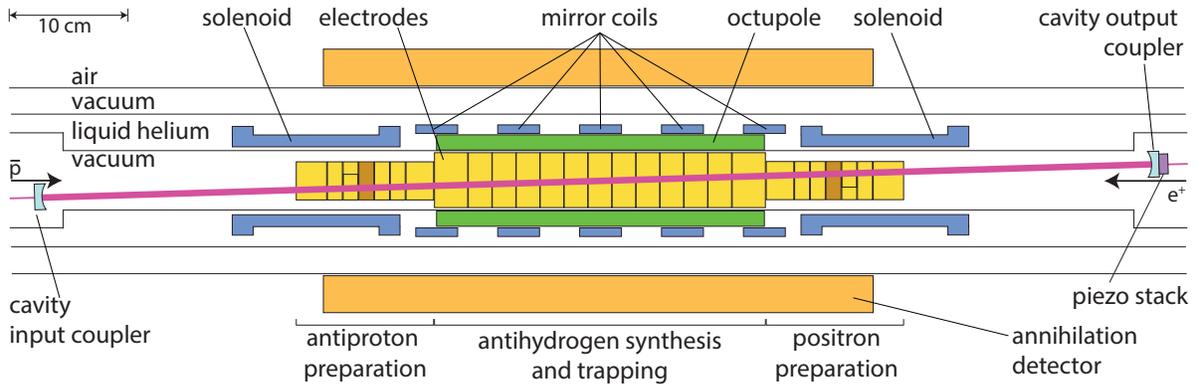
3

FIG. 1. ALPHA experimental setup for antihydrogen synthesis, trapping and spectroscopy. The external main solenoid is not shown. The mirror coils and the octupole are used for antihydrogen trapping, the two solenoids for preparation of antiprotons, positrons and electrons. The drawing also shows the position of the internal build-up cavity mirrors and the external annihilation detector. The drawing is to scale, except for the radial extent of the annihilation detector.

that are at about $2.3°$ to the axis. The path for $1S$-$2S$ light through the trap includes a resonator to allow both for counter-propagating light (this eliminates the first-order Doppler shift) and for building up the intensity of light seen by the anti-atoms. More details on why these features are required will follow in subsequent sections.

Trapped antihydrogen is typically detected through its release and subsequent annihilation on impact on the walls of the apparatus (e.g. the electrodes forming the Penning-Malmberg trap). In ALPHA, the super conducting magnets that form the minimum-B trap are conceived in such a way that they can be de-energised with a decay time of ~ 9 ms. The trap is thus reduced to less than one percent of the original depth in ~ 30 ms, and this time window is the one in which annihilations are looked for [11]. In recent measurements, the ramp-down time of the trap has been increased to 1500 ms, adapting to an increase in the trapping rate which eliminates the need for the high background suppression obtained using the 30 ms shutdown. The slower shutdown avoids the inductive heating of the electrodes as well as the magnet quench caused by the 30 ms ramp-down and allows the trap to be re-energized sooner after the shutdown. In this paper, we will assume that the 1500 ms ramp down is used for detecting antihydrogen in the trap. When this procedure is performed post laser excitation, it is used to detect a decrease in the remaining number of trapped

4

87 anti-atoms and is referred to as disappearance.

88   In ALPHA, annihilations are detected using a silicon strip based vertex detector (the
89 annihilation detector) having three layers of silicon strip detectors that detect the passage
90 of charged particles [12]. By looking at the hit pattern in the detector the tracks of the
91 annihilation products (pions) may be reconstructed and the annihilation vertex (location)
92 determined [13]. The positron annihilates predominantly into two back-to-back photons (at
93 511 keV) but these are not detected in ALPHA. Instead antihydrogen is distinguished from
94 bare antiprotons by (a) preemptively ejecting any remaining charged particles before the
95 minimum-B trap is de-energised and (b) erecting an axial electric (bias) field before the
96 de-energisation. The bias field allows subsequent analysis to determine if the annihilation
97 observed was from a neutral ($\bar{\text{H}}$) or a charged ($\bar{\text{p}}$) particle [14]. Relatively fast de-energisation
98 is important for this endeavour as the detector also has a background rate of false positives
99 from cosmic rays. In the most recent analysis [2], which we will refer to in this paper, two
100 analysis regimes were used, one in which the full annihilation vertex reconstruction efficiency
101 was (68.8±0.2)% with a background rate of 0.042±0.001 s^{-1}, and one in which the recon-
102 struction efficiency was (37.6±0.2)% with a background rate reduced to 0.0043±0.0003 s^{-1}.
103 The former was used for analysing the 1500 ms ramp down of the neutral trap (disappear-
104 ance), giving a background of 0.062 events per trial, whereas the latter was used for searching
105 for annihilations during the long laser exposure periods - referred to as appearance. The
106 false-positive rate of 0.062 events per trial in disappearance is sufficient for the typical trap-
107 ping rates of ∼20 per trial. To observe the resonant loss of antihydrogen atoms due to a
108 $1S$-$2S$ transition it was necessary to observe in the full laser exposure time window of 600 s.
109 To make this possible the appearance analysis regime was used with a background of only
110 2.6 false-positives per 600s window, low enough that a clear $\bar{\text{H}}$ signal could be detected with
111 11 trials, and on average 7 atoms ejected in each on-resonance trial [2]. When considering
112 laser-spectroscopy and what methodology to apply we need to include these considerations.

113   Spectroscopic investigation of the $1S$-$2S$ state of $\bar{\text{H}}$ requires that the $\bar{\text{H}}$ be in its ground
114 state. There is ample experimental evidence that $\bar{\text{H}}$ is predominantly formed through the
115 three body process where two positrons undergo a simultaneous collision with an antiproton
116 such that one is captured [5]. As the energy exchange is in the $T_{e^+} k_B$ range, the nascent
117 $\bar{\text{H}}$ is weakly bound (and many field-ionize on the trap electric fields [15]), and it has been
118 estimated that it takes about 1 s for almost all to have decayed to the ground state [16].

119 Once trapped and in its ground state the antihydrogen is stable as demonstrated by the long
120 observed confinement times [2, 11]. However, in Ref. [11], it was also found that the observed
121 energy distribution of the trapped H̄ was consistent with a 50 K distribution truncated by
122 the trap depth. This means that many anti-atoms will be probing the full trap that has a
123 total volume of about 400 cm³.

124 How to probe the $1S$-$2S$ two-photon transition with only a few antihydrogen atoms
125 moving in such a large volume is the challenge that we are exploring in the following.

126 **III.   ENERGY LEVELS OF (ANTI)HYDROGEN**

127 We need to calculate the energies of states in the (anti)hydrogen atom for two purposes.
128 Firstly, we want to know the transition frequency of the $1S$-$2S$ transition that we will be
129 driving. Since both the transition and the excitation laser have a narrow line width, we need
130 to be quite accurate in this calculation and we will include effects of size down to about one
131 kHz as that is the current limit of what we expect to be able to do experimentally. Secondly,
132 in order to determine shifts of the $2S$ sub-states and the lifetime, we need to calculate the
133 interactions between $2S$ and $2P$. Again, the driving factor is to keep the influence on the
134 precision to about one kHz.

135 In the following, when we refer to energy in units of Hz, it is assumed to be multiplied
136 by Planck's constant (h).

137 **A. $1S$-$2S$ Transition Frequency**

138 To get the transition frequencies between the individual hyperfine states of the $1S$ and
139 $2S$ levels, we will calculate the hyperfine state energies with respect to the level centroid as
140 functions of the magnetic field. We can then add the experimentally determined centroid
141 to centroid energy difference from [1] to obtain the total transition frequency in a magnetic
142 field.

Ignoring for the moment the diamagnetic term, we express the hyperfine hamiltonian for
the S states in terms of the antiproton spin $\vec{I}$, the positron spin, $\vec{S}$, and the magnetic field,

6

$\vec{B}$:

$$H = \frac{\mathcal{E}_{HF}}{\hbar^2}\left(\vec{I}\cdot\vec{S}\right) + \left(-\frac{\mu_e(n)}{\hbar}\vec{S} + \frac{\mu_p}{\hbar}\vec{I}\right)\cdot\vec{B} \tag{1}$$

143 where μ_p is the (anti)proton magnetic moment and $\mathcal{E}_{HF}$ is the zero-field hyperfine splitting
144 for the principal quantum number (n) under consideration.

We have let the positron magnetic moment carry a dependence of the primary quantum number, since μ_e scales with the binding energy of the positron. For the S states, this dependence is [17]:

$$\mu_e(n) = \mu_e\left(1 - \frac{\alpha^2}{3n^2}\right) \tag{2}$$

145 where μ_e is then the magnetic moment of the unbound positron, and α is the fine structure
146 constant.

The eigenvalues of (1) can be found analytically, resulting in the Breit-Rabi formula:

$$\mathcal{E}_{F=I\pm 1/2} = -\frac{\mathcal{E}_{HF}}{4} - \mu_p m_F B \pm \frac{\mathcal{E}_{HF}}{2}\sqrt{1 + 2m_F x + x^2} \tag{3}$$

$$x = \frac{B\left(\mu_e(n) + \mu_p\right)}{\mathcal{E}_{HF}} \tag{4}$$

147 where m_F is the z-component of the total spin. In the case of $m_F = -1$, the square root
148 contains a complete square and the $+(1-x)$ solution is taken.

149 Now to add back in the diamagnetic term, $H' = \frac{e^2}{8m}B^2(x^2 + y^2)$, that was left out in (1),
150 we get from first order perturbation theory:

$$\mathcal{E}_{dia,1S} = \langle 1S|\,H'\,|1S\rangle = \frac{e^2 a_0^2}{4m}B^2 \simeq 29.8\,\text{kHz}\,(B/1\text{T})^2 \tag{5}$$

$$\mathcal{E}_{dia,2S} = \langle 2S|\,H'\,|2S\rangle = \frac{7e^2 a_0^2}{2m}B^2 \simeq 416.7\,\text{kHz}\,(B/1\text{T})^2 \tag{6}$$

151 where a_0 is the Bohr radius, m is the electron mass and e is the fundamental charge.

In Figure 2, the energies of each of the hyperfine states are shown as a function of the magnetic field. We adopt the traditional naming of these states: from $|a\rangle$ to $|d\rangle$ in order of increasing energy. Only states $|c\rangle$ and $|d\rangle$ can be trapped in a magnetic minimum, so $1S_c - 2S_c$ and $1S_d - 2S_d$ are the only transitions we need to consider. Writing these out explicitly, we have:

$$\mathcal{E}_{d-d} = \mathcal{E}_{1S2S} - \frac{\mathcal{E}_{HF}(1) - \mathcal{E}_{HF}(2)}{4} + \frac{\mu_e(2) - \mu_e(1)}{2}B + \frac{13e^2 a_0^2}{4m}B^2 \tag{7}$$

$$\mathcal{E}_{c-c} = \mathcal{E}_{1S2S} + \frac{\mathcal{E}_{HF}(1) - \mathcal{E}_{HF}(2)}{4} + \frac{13e^2 a_0^2}{4m}B^2$$
$$-\frac{1}{2}\sqrt{\mathcal{E}_{HF}(1)^2 + (\mu_e(1) + \mu_p)B^2} + \frac{1}{2}\sqrt{\mathcal{E}_{HF}(2)^2 + (\mu_e(2) + \mu_p)B^2} \tag{8}$$
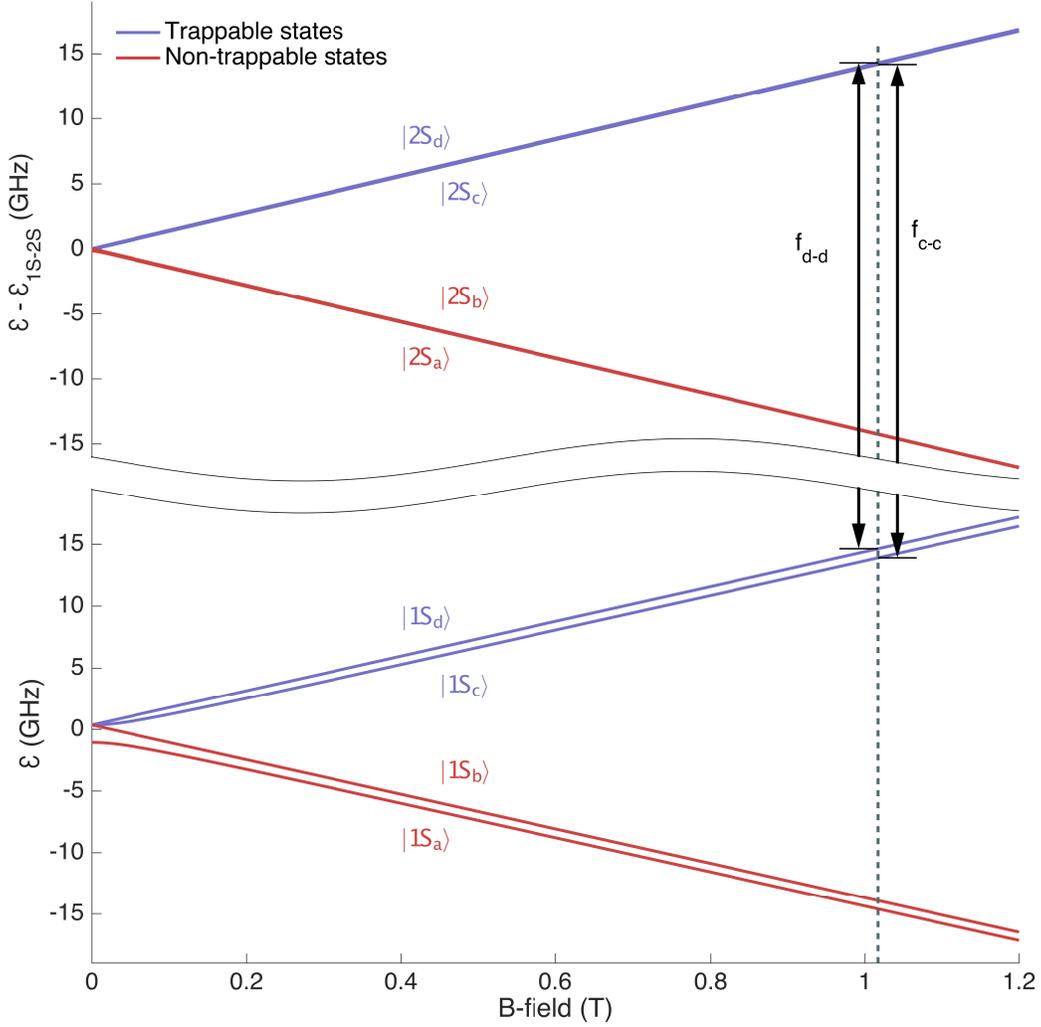
FIG. 2. Hyperfine structure of the $1S$- and $2S$- states in (anti)hydrogen. Diamagnetic states ($|c\rangle$ and $|d\rangle$), also called low-field seekers, can be magnetically trapped. Indicated with black arrows are the two $1S$-$2S$ transitions available in magnetically trapped antihydrogen.

B. 2P States

To understand the behavior of the excited $2S$ atom, we will need to consider mixing with the nearby $2P$ states. Since both the energy differences and spin content are altered significantly by the strong magnetic fields of interest, we start by calculating the states and their energies in the magnetic field. The Hamiltonian for the $2P$ states is approximated by:

$$H = \mathcal{E}_{2P_{1/2}} + \frac{2}{3}\mathcal{E}_{FS}\left(\frac{\vec{L}\cdot\vec{S}}{\hbar^2} + 1\right) - \frac{e\hbar}{2m}\frac{\vec{L}\cdot\vec{B}}{\hbar} - \mu_e\frac{\vec{S}\cdot\vec{B}}{\hbar} \tag{9}$$

8

where $\mathcal{E}_{FS}$ is the splitting between the $2P_{1/2}$ and $2P_{3/2}$ states at zero magnetic field. We have neglected the magnetic moment of the antiproton and we equally ignore a number of other effects that are much smaller than the typical energy differences between 2P and 2S states. In the $|m_l, m_s\rangle$ basis, the two maximally polarized states, $|a\rangle = |-1, -1/2\rangle$ and $|d\rangle = |1, 1/2\rangle$ are also eigenvectors of H, while the rest get mixed by the spin-orbit interaction, $\vec{L} \cdot \vec{S}$. The projection of the total angular momentum, $m_J = m_l + m_s$ is conserved, so we need only simultaneously diagonalize states with the same value for m_J. The eigenvalues are:

$$\mathcal{E}_a = \mathcal{E}_{2P_{1/2}} + \mathcal{E}_{FS} + \mu_e B$$
$$\mathcal{E}_b = \mathcal{E}_0(B) + \mathcal{E}_1(B)$$
$$\mathcal{E}_c = \mathcal{E}_0(-B) + \mathcal{E}_1(-B) \qquad (10)$$
$$\mathcal{E}_d = \mathcal{E}_{2P_{1/2}} + \mathcal{E}_{FS} - \mu_e B$$
$$\mathcal{E}_e = \mathcal{E}_0(B) - \mathcal{E}_1(B)$$
$$\mathcal{E}_f = \mathcal{E}_0(-B) - \mathcal{E}_1(-B)$$

where we have defined the energies:

$$\mathcal{E}_0(B) = \mathcal{E}_{2P_{1/2}} + \frac{1}{2}\mathcal{E}_{FS} + \frac{1}{4}\mu_e B \qquad (11)$$

$$\mathcal{E}_1(B) = \sqrt{\left(\frac{1}{6}\mathcal{E}_{FS} + \frac{1}{4}\mu_e B\right)^2 + \frac{2}{9}\mathcal{E}_{FS}^2} \qquad (12)$$

The corresponding eigenstates are

$$|2P_a\rangle = |-1, -1/2\rangle$$
$$|2P_b\rangle = |0, -1/2\rangle \cos\tau + |-1, 1/2\rangle \sin\tau$$
$$|2P_c\rangle = |0, 1/2\rangle \cos\sigma + |1, -1/2\rangle \sin\sigma$$
$$|2P_d\rangle = |1, 1/2\rangle \qquad (13)$$
$$|2P_e\rangle = |-1, 1/2\rangle \cos\tau - |0, -1/2\rangle \sin\tau$$
$$|2P_f\rangle = |1, -1/2\rangle \cos\sigma - |0, 1/2\rangle \sin\sigma$$

where τ and σ are mixing angles given by

$$\tan\tau = \frac{6\mathcal{E}_1(B) - \frac{3}{2}\mu_e B - \mathcal{E}_{FS}}{2\sqrt{2}\mathcal{E}_{FS}} \qquad (14)$$

$$\tan\sigma = \frac{6\mathcal{E}_1(-B) + \frac{3}{2}\mu_e B - \mathcal{E}_{FS}}{2\sqrt{2}\mathcal{E}_{FS}} \qquad (15)$$

₁₅₇ In the limit of large B-fields, τ tends to 0, while σ tends to $\pi/2$. Figure 3 shows the energies

₁₅₈ of these states as a function of the magnetic field as well as those of the $2S$ states.
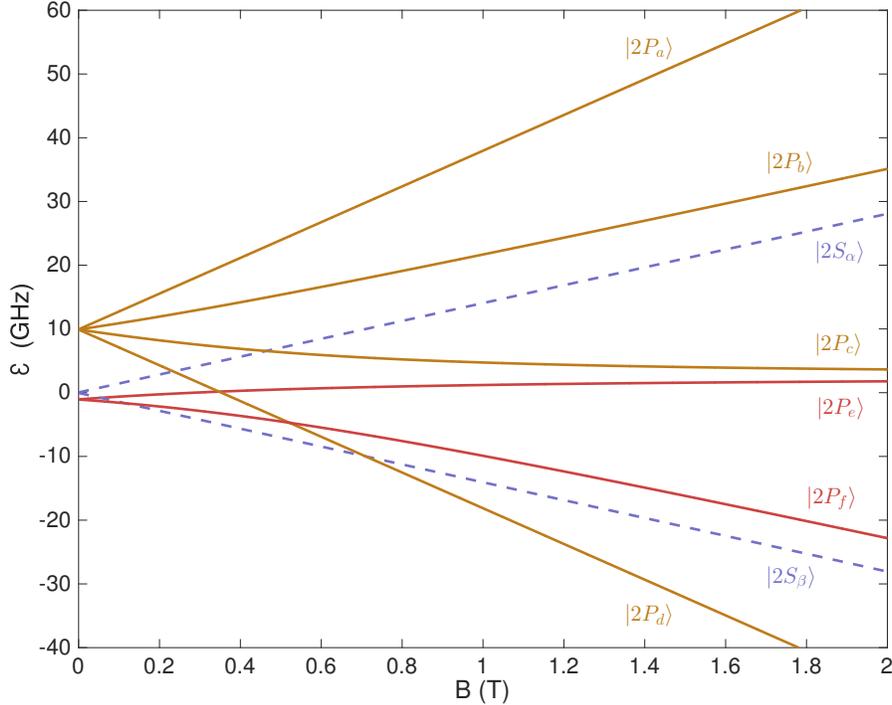

FIG. 3. Fine structure splitting of the $n = 2$ manifold. The $2P$ states are named with subscripts a through f in order of decreasing energy at low magnetic fields. We label the $2S$ states with the subscripts α and β for low- and high-field seekers, ignoring the hyperfine splitting.

₁₅₉ ## C. Mixing and Decay Rates

The $2S$ state of (anti)hydrogen is metastable with a natural lifetime of $\sim 120\text{ms}$. In an external electric field however, the $2S$ state is mixed with the $2P$ states, allowing a single photon decay to the ground state. Since this can limit the time available for detecting the excited $2S$ atoms, we calculate the modified decay rate of the $2S$ state in an electric field. Consider first a system of a $2S$ state and a single $2P$ state and an electric interaction between them, $U = \langle 2P| - e\,\vec{r} \cdot \vec{E}\,|2S\rangle$. With the $2S$ energy as zero point, we can write the Hamiltonian of the system with an electric field as:

$$H = \begin{bmatrix} 0 & U \\ U & -\mathcal{E}_P - i\hbar\gamma_P/2 \end{bmatrix} \tag{16}$$

10

Here we have introduced the decay rate of the $2P$ state as an imaginary part to its energy. We ignore the decay rate of the unmodified $2S$ state for now. The states modified by the electric field are the eigenstates of this matrix, and we can find the decay rate of the modified $2S'$ state from the imaginary part of the corresponding eigenvalue. This eigenvalue is:

$$\mathcal{E}_{2S'} = \frac{1}{2}\left(\mathcal{E}_P + i\hbar\gamma_P/2\right)\left(-1 + \sqrt{1 + \frac{4U^2}{(\mathcal{E}_P + i\hbar\gamma_P/2)^2}}\right)$$

$$\approx \mathcal{E}_P \frac{U^2}{(\mathcal{E}_P^2 + \hbar^2\gamma_P^2/4)} - i\hbar\gamma_P/2 \frac{U^2}{(\mathcal{E}_P^2 + \hbar^2\gamma_P^2/4)} \tag{17}$$

We expanded the square root for small values of the fraction inside. In particular, the electrical interaction, U remains much smaller than $\mathcal{E}_P$ for any fields that we will consider. Note however in Figure 3, that around $B = 0.5$ T, the magnetic field introduces a degeneracy between the trappable $2S$ state and the $2P_c$ state. The decay rate in any other field is then given by $-2/\hbar$ times the imaginary part of this energy:

$$\gamma_{2S'} = \gamma_P \frac{U^2}{(\mathcal{E}_P^2 + \hbar^2\gamma_P^2/4)} \tag{18}$$

To get the total decay rate, we have to add the contributions from each of the $2P$ states. We will consider the general case of an arbitrary angle between $\vec{E}$ and $\vec{B}$, so we let the Hamiltonian for the electric field be given by

$$H'_E = -e\left(xE_\perp + zE_\parallel\right) \tag{19}$$

We then calculate the matrix elements with each of the $2P$ states, $U_i = \langle 2P_i| H'_E |2S\rangle$. The total single photon decay rate of our modified $2S'$ state can then be written as:

$$\gamma_{2S'} = \gamma_{2P} \sum_i \left[\frac{U_i^2}{(\mathcal{E}_{P,i}^2 + \hbar^2\gamma_{2P}^2/4)}\right] \tag{20}$$

$$\overset{1\mathrm{T}}{\approx} 0.015\,\mathrm{s}^{-1}\left(\frac{E_\parallel}{\mathrm{V/m}}\right)^2 + 0.0055\,\mathrm{s}^{-1}\left(\frac{E_\perp}{\mathrm{V/m}}\right)^2 \tag{21}$$

where the second line is evaluated at $B = 1\,\mathrm{T}$. Realistic decay rates for 2S atoms in the ALPHA trap are estimated below.

D. Decays with Spin-flip

Each of the $2P_i$ states can decay with a single photon to either a trappable hyperfine state ($|1S_c\rangle$ or $|1S_d\rangle$), or an untrappable one ($|1S_a\rangle$ or $|1S_b\rangle$). The probability for each is given

11

by the amount of positron spin in the $2P_i$ state that matches the ground state in question. For each of the $2P_i$ states, we can thus assign a probability $P_i(B)$ that this state will decay into an untrappable 1S state. It is a function of the magnetic field since the composition of pure spin states in the $2P_i$ states depends on B, see equation (13). We can now write up the probability for a trappable $2S$ atom, which decays through a $2P$ state by mixing in an electric field, to result in an untrappable $1S$ state. This probability is simply the fraction of the spin-flipping decay rate to the total single photon decay rate:

$$\beta_{\text{spinflip}} = \frac{\gamma_{2P}}{\gamma_{2S'}} \sum_i \left[\frac{P_i U_i^2}{(\mathcal{E}_{P,i}^2 + \hbar^2 \gamma_{2P}^2/4)} \right] \tag{22}$$

163 where the $\gamma_{2S'}$ is from eqn. (20).

164   In Figure 4 we plot this ratio for both a purely perpendicular electric field, $\vec{E} = (E_\perp, 0, 0)$
165 and a purely parallel one $\vec{E} = (0, 0, E_\parallel)$. At low fields, it is possible to choose the direction
166 of the electric field (parallel to $\vec{B}$) such that a quite high probability of decaying into un-
167 trappable states is achieved. However, as the magnetic field increases, the energy difference
168 between spin directions increases, and these spin-flips become unlikely for any direction of
169 the electric field.

170 **E. $\vec{v} \times \vec{B}$ Decay**

171   An atom moving in a magnetic field will experience an electric field, which will modify
172 the lifetime of the $2S$ state according to (20). Estimating the worst case, the fastest trapped
173 atoms in ALPHA have a kinetic energy of approximately $0.5\,\text{K}$, corresponding to a velocity
174 of about $90\,\text{m/s}$. Assuming this velocity is perpendicular to a $1\,\text{T}$ magnetic field, the electric
175 field in the frame of the atom is

$$|E| = \left| \vec{v} \times \vec{B} \right| = 90 \text{ V m}^{-1}$$

176 In this case, the decay rate in (20), from the purely perpendicular E-field, is $\gamma_{2S'} = 44\,\text{s}^{-1}$.
177 This adds to the two-photon decay rate of $8.2\,\text{s}^{-1}$, which stays practically unaltered by the
178 perturbing electric field. A more realistic estimate can be derived from simulating the atom
179 trajectories in the magnetic field as we will describe below. In these simulations the average
180 decay rate induced by the motional electric field is $11.5\,\text{s}^{-1}$.
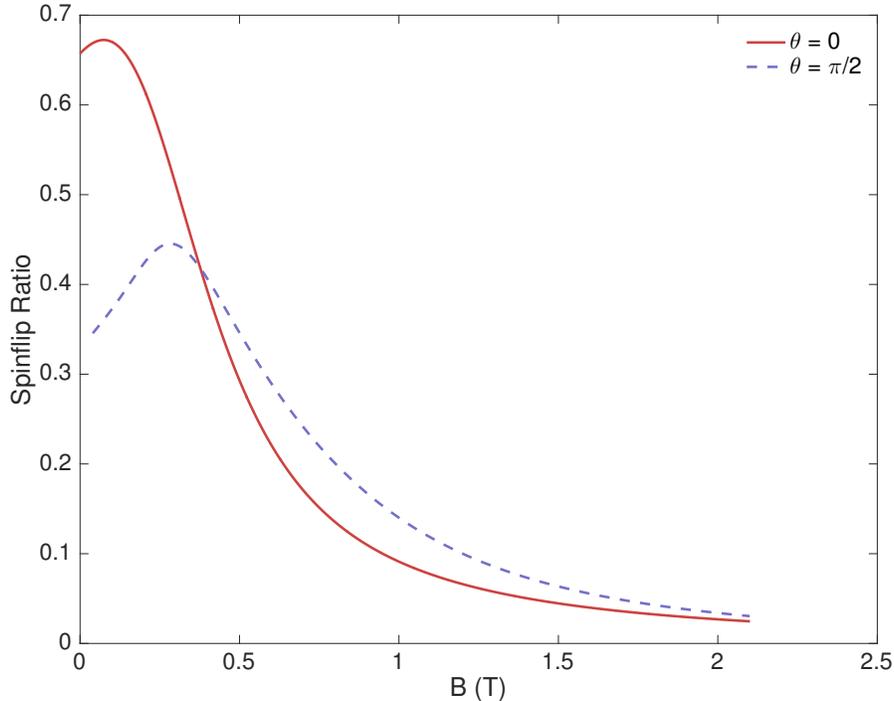
FIG. 4. Ratio of spinflip-inducing single photon $2S$ decays as a function of the magnetic field. Plotted for both $\vec{E} \perp \vec{B}$ ($\theta = \pi/2$) and $\vec{E} \parallel \vec{B}$ ($\theta = 0$). As the magnetic field increases, the states become increasingly spin-polarized, and the probability for changing the spin in a decay decreases for any relative direction of $\vec{B}$ and $\vec{E}$.

IV. 1S-2S EXCITATION

We now turn to deriving the equations that govern the two photon excitation from the $1S$ to the $2S$ state. We will need to make some assumptions of experimental conditions, and will base all of these on the situation in ALPHA.

The designed beam waist of approximately $w_0 = 200\,\mu$m implies a Rayleigh range of $z_R = \pi w_0^2 / \lambda \approx 50\,$cm, which is much larger than the $\sim 6\,$cm long flat region of the magnetic trap containing the $\bar{\text{H}}$. This means that we can ignore the change in beam size with position when calculating a single pass through the laser. In the full simulation of the experiment described below, we include the shape of the laser beam by assigning the appropriate width of laser beam to each beam crossing.

We will also assume a monochromatic laser beam. This assumption is good if the laser line width is small compared to the inverse of the transit time of the atoms through the laser

beam, which is the case for ALPHA. Thus, the standing wave electric field we consider is:

$$\vec{E} = \hat{x}E_0 e^{-r^2/w^2}\cos(kz + \delta)\cos(\omega_L t) \tag{23}$$

where $r^2 = x^2 + y^2$, w is the beam waist, δ is a phase shift which has no effect on the calculation, E_0 is the maximum electric field, and $\omega_L/(2\pi)$ is the laser frequency. Thinking of the standing wave as a superposition of light moving in the $+z$ direction and in the $-z$ direction, the intensity of light in *one* of the beams is $I = c\varepsilon_0 E_0^2/8$. For a Gaussian beam, $I = 2P_0/(\pi w^2)$ where P_0 is the total power in one beam.

The two photon excitation of the 2S state occurs by a virtual excitation through the nP states. Because the one photon absorption is far off resonance from any P state, the infinite number of P states can be adiabatically eliminated from the equations. We will write the wave function as

$$|\Psi(t)\rangle = |\psi_{1S}\rangle\, e^{-i\mathcal{E}_{1S}t/\hbar}C_{1S}(t) + \sum_n |\psi_{nP}\rangle\, e^{-i\mathcal{E}_{nP}t/\hbar}C_{nP}(t) \tag{24}$$

$$+ |\psi_{2S}\rangle\, e^{-i\mathcal{E}_{2S}t/\hbar}C_{2S}(t) \tag{25}$$

where the Cs are slowly varying coefficients and the sum over n is understood to also include the continuum states. Substituting into the Schrödinger equation gives:

$$i\hbar\frac{dC_{1S}}{dt} = eE_x(\vec{r}(t),t)\sum_n D_{1S,nP}e^{-i(\mathcal{E}_{nP}-\mathcal{E}_{1S})t/\hbar}C_{nP} \tag{26}$$

$$i\hbar\frac{dC_{nP}}{dt} = eE_x(\vec{r}(t),t)\left[D_{nP,1S}e^{-i(\mathcal{E}_{1S}-\mathcal{E}_{nP})t/\hbar}C_{1S} + D_{nP,2S}e^{-i(\mathcal{E}_{2S}-\mathcal{E}_{nP})t/\hbar}C_{2S}\right]$$

$$i\hbar\frac{dC_{2S}}{dt} = eE_x(\vec{r}(t),t)\sum_n D_{2S,nP}e^{-i(\mathcal{E}_{nP}-\mathcal{E}_{2S})t/\hbar}C_{nP}$$

where the electric field is from Equation (23), and $D_{k,l}$ denotes the electric dipole moment between states k and l.

These are fairly complicated equations so we will perform some simplifications based on the situation we're modeling. First, we are interested in the two photon absorption from a laser beam that is weak on the scale of the atomic parameters. This means the counter-rotating terms in the electric field can be dropped. Second, the time dependence in the electric field due to the changing position of the $\bar{\text{H}}$ can *not* be dropped; the time dependence of z gives the Doppler shift and the time dependence in x, y gives the rise and fall of the intensity. However, because the natural line width of the transition is so small,

14

the $\exp[ikz(t)]$ in going from the $1S$ to the P states must be matched with the $\exp[-ikz(t)]$
when going from the P to the $2S$ state, otherwise the transition will be Doppler shifted out
of resonance.

The middle equation can be approximately solved by integrating both sides with respect
to t and using the fact that the C_{nS} are slowly varying:

$$C_{nP} \simeq -\frac{E_0}{2} e^{-r^2(t)/w^2} \cos{(kz(t))} \left[\frac{D_{nP,1S}}{\mathcal{E}_{nP} - \mathcal{E}_{1S} - \hbar\omega_L} e^{i(\mathcal{E}_{nP} - \mathcal{E}_{1S} - \hbar\omega_L)t/\hbar} C_{1S} \right.$$
$$\left. + \frac{D_{nP,2S}}{\mathcal{E}_{nP} - \mathcal{E}_{2S} + \hbar\omega_L} e^{i(\mathcal{E}_{nP} - \mathcal{E}_{2S} + \hbar\omega_L)t/\hbar} C_{2S} \right] \tag{27}$$

As described in the previous paragraph, when this form is substituted into the equations
for the C_{nS}, the terms that lead to $\exp[\pm 2ikz(t)]$ are dropped because the Doppler shift
makes them non-resonant. The AC Stark shift is described separately in Section V, so here
we will drop those terms. This means ignoring terms with C_{1S} in the dC_{1S}/dt equation and
similarly for the $2S$ state. This leads to the equations that couple the $1S$ and $2S$ states:

$$i\hbar\frac{dC_{1S}}{dt} = \xi E_0^2 e^{-2r^2(t)/w^2} e^{-i(\mathcal{E}_{2S} - \mathcal{E}_{1S} - 2\hbar\omega_L)t/\hbar} C_{2S} \tag{28}$$
$$i\hbar\frac{dC_{2S}}{dt} = \xi E_0^2 e^{-2r^2(t)/w^2} e^{i(\mathcal{E}_{2S} - \mathcal{E}_{1S} - 2\hbar\omega_L)t/\hbar} C_{1S} \tag{29}$$

The parameter ξ is defined as

$$\xi = -\frac{e^2}{8} \sum_n \frac{D_{2S,nP} D_{nP,1S}}{\mathcal{E}_{nP} - \mathcal{E}_{1S} - \hbar\omega_L} \simeq 12.3\varepsilon_0 a_0^3 \tag{30}$$

where the numerical value was obtained by performing the sum using states confined within
a sphere of radius $30\,a_0$.

A. Perturbative Calculation

From (29), we can obtain a simple expression for the excitation probability in a single
pass of the laser, by assuming that this probability is small and set $C_{1S} = 1$. This leaves us
with a single, uncoupled equation for C_{2S} that we can integrate over the traversal of the laser
beam. For this calculation we choose coordinates such that the laser axis coincides with the
z-axis, and we define the detuning, $\Delta = 2\omega_L - (\mathcal{E}_{2S} - \mathcal{E}_{1S})/\hbar$, as well as the perpendicular
velocity, $v_\perp^2 = v_x^2 + v_y^2$. We let the closest approach to the axis happen at $t = 0$ and call this

15

distance b, so $r^2(t) = b^2 + v_\perp^2 t^2$. We can now write the coefficient of the $2S$ state as:

$$C_{2S} = \frac{\xi}{i\hbar} E_0^2 e^{-2b^2/w^2} \int_{-\infty}^{\infty} e^{-2v_\perp^2 t^2/w^2} e^{-i\Delta t} \, dt \tag{31}$$

$$= \frac{\xi}{i\hbar} E_0^2 e^{-2b^2/w^2} \frac{w}{v_\perp} \sqrt{\frac{\pi}{2}} e^{-\frac{\Delta^2 w^2}{8v_\perp}} \tag{32}$$

For the excited population, we recast the laser parameters in terms of more directly measurable quantities: the laser frequency, f, the resonant frequency for the two-photon transition, $f_0 = (\mathcal{E}_{2S} - \mathcal{E}_{1S})/2h$, and the maximum intensity in the single direction laser beam, I.

$$|C_{2S}|^2 \simeq 32\pi I^2 \frac{12.3^2 a_0^6}{\hbar^2 c^2} \frac{w^2}{v_\perp^2} e^{-4b^2/w^2} e^{-(f-f_0)(2\pi w/v_\perp)^2} \tag{33}$$

Suppose now that the laser frequency is different for each crossing of the laser beam, emulating the case of some laser line width with a characteristic time scale longer than a single crossing. Taking the frequencies for each pass from a Gaussian distribution with a FWHM of δf_{las} around the central f_{las}, we get the average excitation:

$$< |C_{2S}|^2 > = \frac{\sqrt{8\ln 2}}{\sqrt{\pi}\, \delta f_{las}} \int_{-\infty}^{\infty} |C_{2S}|^2(f)\, e^{-8\ln 2 (f-f_{\text{las}})^2/\delta f_{\text{las}}} \, df \tag{34}$$

$$= \frac{16I^2}{\delta f} \frac{12.3^2 a_0^6}{\hbar^2 c^2} \frac{w}{v_\perp} e^{-4b^2/w^2} e^{-(f_0 - f_{\text{las}})/\delta f^2} \tag{35}$$

where we have now introduced $\delta f^2 = (\frac{v_\perp}{2\pi w})^2 + \frac{\delta f_{\text{las}}^2}{8\ln 2}$, which is simply the laser width and the transit time width added in quadrature.

Thus, in (35) we have arrived at the excitation probability in a single pass, incorporating both the dominating broadening mechanism and the laser linewidth, in a single perturbative expression.

B.   Density Matrix Formalism

Above, we made the perturbative assumption that the population in the ground state does not change in a single pass of the laser beam. Although this is a reasonable assumption for realistic experimental parameters, we need to also account for photo-ionisation of the $2S$ state as well as effects of the position dependence of its lifetime. To do this we turn to the density matrix formulation, in which the time evolution of the density operator, ρ, is

16

described by the von Neumann equation:

$$\dot{\rho} = -\frac{i}{\hbar}\left(H\rho - \rho H\right) \qquad (36)$$

We consider the 4 states: $|1\rangle$ is the low field seeking $1S$ state, in which we initially place the entire population. $|2\rangle$ is the high field seeking $1S$ state, which can be produced in decays from $2S$ states, and is unconfined by the magnetic trap. $|3\rangle$ is the photo-ionised state with the positron dissociated from the antiproton. We will neglect the possibility of direct 3-photon ionisation of the $1S$ state. Finally, $|4\rangle$ is the low field seeking $2S$ state, with the laser interaction coupling states $|1\rangle$ and $|4\rangle$.

We explicitly introduce decay rates for the relevant channels out of the $2S$ state. Γ_{41} includes both the two photon decays, which conserve the hyperfine state, as well as the fraction of single photon decays induced by mixing with $2P$ states which do not alter the spin direction of the positron. The single photon decays that flip the positron spin constitute Γ_{42}. We calculated the single photon decay rate as well as the spin-flip ratio in these decays in equations (20) and (22), including their dependence on the electric and magnetic fields. Γ_{43} is the rate of photo-ionisation by $243\,\mathrm{nm}$ photons, which is proportional to the local density of those photons. Solving numerically for this rate, we get:

$$\Gamma_{43} = 7.57\ \mathrm{s}^{-1}\frac{I}{\mathrm{W/cm}^2} \qquad (37)$$

Assembling this into the density matrix formalism, we can write out the non-zero and non-trivial entries of $\dot{\rho}$

$$\dot{\rho}_{11} = -\frac{i}{2}\Omega_{14}(t)\left(\rho_{41} - \rho_{14}\right) + \Gamma_{41}\rho_{44}$$

$$\dot{\rho}_{22} = \Gamma_{42}\rho_{44}$$

$$\dot{\rho}_{33} = \Gamma_{43}\rho_{44} \qquad (38)$$

$$\dot{\rho}_{44} = -\frac{i}{2}\Omega_{14}(t)\left(\rho_{14} - \rho_{41}\right) - \Gamma\rho_{44}$$

$$\dot{\rho}_{14} = -\frac{i}{2}\Omega_{14}(t)\left(\rho_{44} - \rho_{11}\right) + \left(-i\Delta - \frac{1}{2}\Gamma\right)\rho_{14}$$

where the equivalent of the Rabi frequency for the two-photon transition is once again derived from (29).

$$\Omega_{14}(t) = 12.3a_0^3\frac{16I}{\hbar c}\mathrm{e}^{-2r(t)^2/w^2} \qquad (39)$$

17

₂₂₄ and we defined $\Gamma \equiv \Gamma_{41} + \Gamma_{42} + \Gamma_{43}$. The detuning is defined, like before, for the two photons

₂₂₅ combined, $\Delta = 2\omega_L - (\mathcal{E}_4 - \mathcal{E}_1)/\hbar$.

₂₂₆

₂₂₇   In Figure 5 we compare the excitation rates of the perturbative expression in (35) and

₂₂₈ that obtained by numerically integrating the equations (38) over a similar crossing of the

₂₂₉ laser beam. For small laser powers, large impact parameters, or large $v_\perp$ the perturbative

₂₃₀ error as well as the ionisation probability, which the expression in (35) does not account

₂₃₁ for, are both negligible. This means that in numerical simulations like the ones described

₂₃₂ in Section VI, computation time can be saved by only integrating the full set of equations

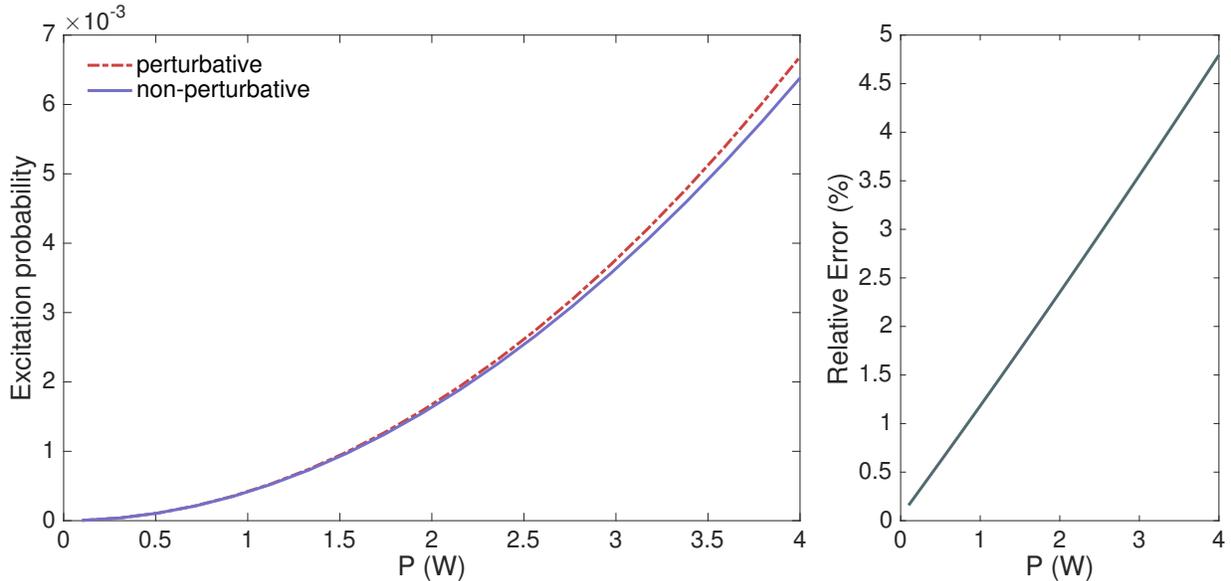₂₃₃ when the maximum intensity seen in a crossing of the laser beam is high.

FIG. 5. Left: Excitation probability in a single pass of the laser beam for both the perturbative

expression (35), and the non-perturbative calculation, where (38) is numerically solved for ρ_{44}.

Assumed is a 200 μm beam waist and a perpendicular velocity of $v_\perp = 90\,\mathrm{m/s}$. Right: The relative

difference between the two methods.

₂₃₄   We are calculating the transition probabilities for intensities of laser light that are higher

₂₃₅ than what have been used in some notable $1S$-$2S$ spectroscopy experiments in hydrogen (see

₂₃₆ Table I for an overview). The main difference between these regular hydrogen experiments

₂₃₇ and ALPHA, which drives the need for high laser power is the number of atoms addressed.

₂₃₈ While a strong signal can be achieved by exciting a very small fraction of 10^{10} atoms,

18

₂₃₉ a single trapped antihydrogen atom must become excited with a high probability for any ₂₄₀ experiment to be feasible.

₂₄₁ It is worth pointing out that a circulating power of 2 W as assumed in some of our ₂₄₂ simulations is well within the capacity for build-up in the enhancement cavity in ALPHA. ₂₄₃ For the most precise $1S$-$2S$ measurements achieved in hydrogen [1], there is little incentive ₂₄₄ to increase the laser intensity, as doing so would increase the size of the AC stark shift, ₂₄₅ which is a leading systematic effect in those experiments.

TABLE I. Laser parameters in selected $1S$-$2S$ spectroscopic measurements in hydrogen and an-tihydrogen. In [1] an enhancement cavity is used to build up laser power, while in [18] a single reflection of the 243 nm beam provides the counter-propagating photons. The number of atoms, N_{H}, quoted for [18] is a trapped and cooled sample, while for [1], where a hydrogen beam is used, we list the flux of atomic hydrogen from the cryogenic nozzle [19]. The intensities listed here are representative for their respective experiments, but as discussed in Section V, the laser intensity can be intentionally varied to compensate for the AC stark shift.

	w_0	P	I_0	N
Parthey et al. 2011 [1] (H)	$292\,\mu$m	$300\,$mW	$2.2\,$MW/m^2	$\sim 10^{16}\,$s^{-1}
Cesar et al. 1996 [18] (H)	$37\,\mu$m	$4\,$mW	$1.9\,$MW/m^2	$10^{10} - 10^{13}$
Ahmadi et al. 2017 [2] ($\bar{\mathrm{H}}$)	$196\,\mu$m	$1000\,$mW	$17\,$MW/m^2	~ 15

₂₄₆ V. SHIFTS AND BROADENING EFFECTS

₂₄₇ In this section we review the broadening effects and shifts relevant for the initial detection ₂₄₈ of a $1S$-$2S$ excitation signal in ALPHA [2], and for a measurement of the transition frequency ₂₄₉ to within a few kHz. We leave out well known effects like the second order Doppler shift, ₂₅₀ which enters only below this level for foreseen experimental parameters. A summary of the ₂₅₁ effects treated and their inclusion in our simulations of the experiment at the current stage ₂₅₂ is given in Table II.

A. Transition Time Broadening

The dominant broadening effect for our current experimental parameters is due to the limited interaction time between the laser beam and an atom passing through it. The uncertainty in laser frequency as seen by the atom moving is inversely proportional to the time it takes to pass through the laser beam. The FWHM of this broadening is:

$$\Delta f_{Transit} = \sqrt{\ln(2)} \frac{v_\perp}{\pi w_0} \tag{40}$$

Since the transition of interest must be driven by two photons with this frequency width, the resulting width in terms of the full transition frequency is twice this expression. The average velocity of trapped antihydrogen atoms in ALPHA is about $75\,\mathrm{m/s}$. Assuming equal velocity components along all 3 axes, the velocity perpendicular to the laser beam is a factor $\sqrt{2/3}$ smaller. Thus, using $v_\perp = 60\,\mathrm{m/s}$ and $w_0 = 196\,\mu\mathrm{m}$, the estimated average transition time broadening is $\sim 160\,\mathrm{kHz}$. In terms of the resulting lineshape, this simple estimate neglects the fact that atoms that move slower contribute a larger transition probability, so the above somewhat overestimates the resulting width.

Transit time broadening is also inherent in experiments on atomic beams, where the interaction time is necessarily limited. It can be reduced greatly in magnetically trapped samples as demonstrated in [18]. It is worth noting though, that this requires a much colder sample of antihydrogen and a tighter magnetic minimum trap than what has been achieved so far, such that the atoms can be contained almost entirely within the laser beam.

B. DC Stark Effect

An external electric field causes mixing between the S- and P- states in (anti)hydrogen which we showed above causes an increse in the decay rate of the $2S$ state. The same mixing leads to an energy shift of both the $1S$ and $2S$ states, which we will treat here. As the trapped atoms will experience a range of electric field strengths from the motional, $\vec{v} \times \vec{B}$ field, the transition is broadened as well as shifted.

The energy shift of the S states is calculated in second order perturbation theory, summing contributions from the P-states. For the $1S$ state, no P-states are near enough that a 1T magnetic field significantly alters any energy difference, so we can use the zero-field polarizabillity:

$$\alpha_{1S} = 4\pi\epsilon_0 \frac{9}{2} a_0^3 \tag{41}$$

which leads to the energy shift:

$$\Delta\mathcal{E}_{1S} = -\frac{1}{2}\alpha_{1S}E^2 \approx -5.6 \times 10^{-8}\,\mathrm{Hz} \left(\frac{E}{\mathrm{V/m}}\right)^2 \tag{42}$$

For the $2S$ state, the shift is dominated by contributions from the nearby $2P$ states, and the energy differences will be heavily influenced by the magnetic field. We therefore need to use the 2P states and energies found in Section III. The perturbing Hamiltonian is the same as we used for calculating the 2S decay rate, (19), and the second order perturbation is then:

$$\Delta\mathcal{E}_{2S} = \sum_k \frac{|\langle k| H_E' |2S\rangle|^2}{\mathcal{E}_{2S} - \mathcal{E}_k} \tag{43}$$

$$\overset{1\mathrm{T}}{\approx} -0.17\,\mathrm{Hz}\left(\frac{E_\parallel}{\mathrm{V/m}}\right)^2 + 0.041\,\mathrm{Hz}\left(\frac{E_\perp}{\mathrm{V/m}}\right)^2 \tag{44}$$

We summed over only the $2P$ states at $B = 1\,\mathrm{T}$ to get the approximate numbers in the second line. This is a good approximation due to the much larger energy difference to all other P states.

Assuming as the worst case possible in the ALPHA trap, a velocity perpendicular to the $1\,\mathrm{T}$ magnetic field of $90\,\mathrm{m/s}$, the shift of the $1S$-$2S$ transition frequency induced by the DC Stark effect from the motional electric field is then $\sim 300\,\mathrm{Hz}$. At the desired level of accuracy, we can thus safely ignore this.

C.   AC stark Effect

The oscillating electric field of the laser also introduces a shift of both the $1S$- and the $2S$- state. This was explicitly left out in Section IV, and we re-introduce this shift at this stage. We arrive at a value for the shift of the total transition frequency (taking the real part of the 2S shift), which coincides with the thorough treatment in [20]:

$$\Delta f_{AC} = 1.67\,\mathrm{Hz}\,\frac{I}{\mathrm{W/cm}^2} \tag{45}$$

With the power P in each of the counter-propagating beams, the central intensity which takes into account the standing wave pattern, is

$$I_0 = \frac{4P}{\pi w_0^2} \tag{46}$$

285 Thus, for a laser power like that achieved in [2], $P = 1\,\mathrm{W}$, the AC stark shift in the center
286 of the laser beam is $\Delta f_{AC} \approx 5\,\mathrm{kHz}$. This is a negligible shift for the very first detection of
287 $1S$-$2S$ excitations in antihydrogen [2], but it is clear that as the precision of measurements in
288 antihydrogen increases, the AC stark shift will become an important systematic. Eventually
289 it will be necessary to compensate for this shift by measuring the line center at several
290 laser intensities. The transition frequency at zero laser intensity can then be found through
291 extrapolation.

292 ## D. Residual Zeeman Effect

In (7) and (8), we calculated the $1S$-$2S$ transition energies for both the trappable hyperfine states as functions of magnetic field. The frequency shift with magnetic field is thus given quite trivially by these equations. Taking only a linear expansion around $B = 1\,\mathrm{T}$, we get:

$$\Delta f_{Z,d-d} \approx 96 \text{ Hz/Gauss} \tag{47}$$

$$\Delta f_{Z,c-c} \approx 1.9 \text{ kHz/Gauss} \tag{48}$$

293 We call this the residual Zeeman effect as the Zeeman shifts of the initial and excited states
294 are nearly identical, leading to a near cancellation of the Zeeman effect in the transition
295 energy. The exact lineshape resulting from these shifts depends on the details of the atomic
296 orbits in the magnetic trap, and we will discuss this residual Zeeman effect a bit further in
297 the context of simulating the atomic orbits in the ALPHA trap.

298 ## E. Lifetime Broadening

The natural linewidth of an atomic transition is simply the inverse of the lifetime of the excited state, and reductions in this lifetime increase the linewidth similarly. We have already calculated the decay rate introduced by the motional electric field, which leads to a negligible broadening. The largest decrease of the $2S$ lifetime possible in the trap comes from the ionisation rate in the laser beam, given in Equation (37). This leads to a position dependent broadening of the linewidth with a FWHM in the center of the beam, assuming

TABLE II. Broadening effects and shifts and their approximate size. Assuming 1 W of circulating 243 nm light in a 200 µm waist, and atoms travelling at 75 m/s with equal components along each axis. We list the size of effect on the total transition frequency rather than in terms of the frequency of the 243 nm laser that drives it.

Effect	Approximate Size	Included in Simulation
1st order Doppler	cancels	no
2nd order Doppler	80 Hz	no
Transition time	160 kHz	yes
AC Stark	5 kHz	yes
DC Stark	150 Hz	no
Magnetic shift d-d (c-c)	96 Hz/G (1.9 kHz/G)	yes
Ionisation width	4 kHz	yes

the same laser parameters as above of:

$$\Delta f_{ion} = \frac{\Gamma_{43}(P = 1\,\text{W})}{2\pi} \approx 4\ \text{kHz} \tag{49}$$

299 Despite the quite high intensity of laser light used, this is still far from the width contributed 300 by transit time broadening.

VI. NUMERICAL SIMULATION

302 The total rate of excitation at any given laser frequency depends on the dynamics of 303 the magnetically trapped atoms. Furthermore, any precision measurement will rely on 304 comparing the measured response to a detailed model of the line shape. A full simulation 305 of the laser interaction including realistic atom trajectories is therefore needed, and we will 306 here briefly describe how we have implemented this.

307 The ALPHA trap is much larger than the de Broglie wavelength of the trapped atoms, 308 allowing us to model the atoms as classical particles moving in a potential defined by $U =$ 309 $-\vec{\mu}\cdot\vec{B}$, where $\vec{\mu}$ is the magnetic moment of the $\bar{\text{H}}$. Since the spin precession frequency of the 310 positron is also much higher than any of the motional frequencies, this is further simplified 311 and we have for a trapped atom: $U = \mu B$. Since we require a long simulation time compared

23

312 to the motion of the atoms, we use a fourth order symplectic integrator [21–23], which has
313 the advantage of maintaining the total mechanical energy for long simulation times. This
314 part of the simulation code has also been used for other studies of trapped antihydrogen in
315 ALPHA like [24], and has been described in that context.

316   The initial conditions of the simulation mimic those of the $\bar{\text{H}}$ atoms in ALPHA: They
317 are launched from within an ellipsoid the size of the positron plasma used for antihydrogen
318 production, and given random velocities taken from a high temperature thermal distribution.
319 This has previously been found [25] to give the best agreement with the temporal distribution
320 of recorded anithydrogen annihilations during the magnetic trap shutdown. We start the
321 atoms in a high enough Rydberg state ($n = 25$) to allow for the influence of the magnetic
322 moment changing during the radiative decay. We subsequently allow the atoms to decay to
323 the ground state during the first couple of seconds of the simulation, updating their magnetic
324 moments appropriately. The laser is then turned on and the atoms still confined at this time
325 form our trapped ensemble.

326   Anytime an $\bar{\text{H}}$ comes close to the laser beam, the code chooses to either evaluate the
327 perturbative expression (35) in the case where the maximum intensity for the crossing is
328 low, or solve the optical Bloch equations (38) along the path of the atom, in the high
329 intensity case. While far from the laser, the $2S$ population is still allowed to decay to $1S$,
330 either with two photons, or through mixing with $2P$ states caused by the motional electric
331 field as described in (20). The code stops if any of 3 conditions are met: 1) the $\bar{\text{H}}$ hits the
332 wall. This can happen either because the atom is in a high-field seeking state after going
333 through a spin-flipping decay, or, in rare cases, atoms launched with slightly higher energy
334 than the minimum well depth can take a while to find the shallowest point in the trap and
335 escape. 2) If the atom is ionised by absorbing a photon while in the $2S$ state. 3) If the
336 designated illumination time has passed. In all cases, the position and internal state of the
337 atom is recorded at the time of stopping the simulation.

338   **A. Detection Rates**

339   In the left panel of Figure 6, we show the output of such a simulation for parameters
340 similar to those used in the first measurement of the $1S$-$2S$ transition in antihydrogen, [2].
341 These are: $P = 1\,\text{W}$, $w_0 = 200\,\mu\text{m}$, and a flattened magnetic field. The laser frequency is
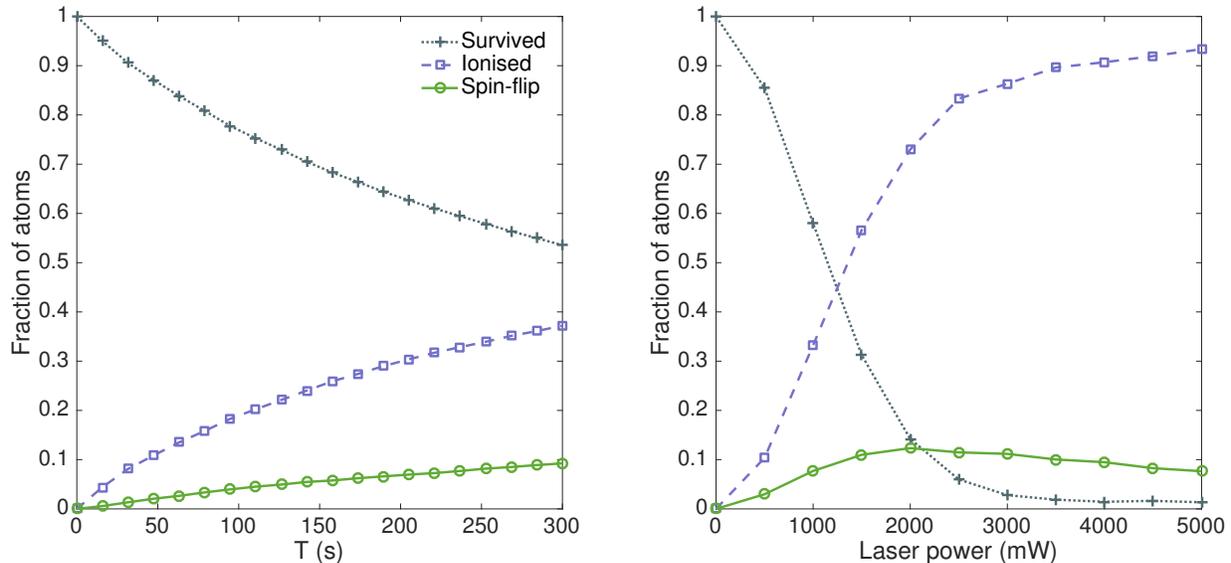
24

FIG. 6. Left: Temporal evolution of simulated atoms during a 300s exposure of with $1000\,\mathrm{mW}$ of laser power. Right: End states of simulated $250\,\mathrm{s}$ exposures at different laser powers. The decrease in spin-flip probability at very high powers can be understood as a competition between the ionisation process, which becomes more efficient with higher photon density, and the spin-flipping decays, which do not.

chosen to be on resonance in the center of the magnetic trap. We plot the total response to illuminating both the c-c and the d-d transitions for the time T, assuming the initial trapped population is evenly distributed between $|1S_c\rangle$ and $|1S_d\rangle$. After illuminating each transition for 300 s, approximately 46 % of the trapped atoms have been eliminated from the trap, either through photo-ionisation or spin-flipping decays. The right panel of Figure 6 shows how the end state of simulated 250s exposures of each transition evolves with laser power, and shows clear effects of saturation at high laser power. The power required to reach this saturation and eliminate nearly all atoms from the trap can naturally be manipulated to some degree by changing the illumination time.

As we will come back to in Section VII, detection of the $1S$-$2S$ excitations can be performed in parallel in both appearance and disappearance mode. One option for providing a direct appearance signal through annihilating the antiprotons resulting from photo-ionisation, and which we will revisit below, involves using one of the five mirror coils to cancel the background 1T field. This will cause the field lines to fan out and force antipro-
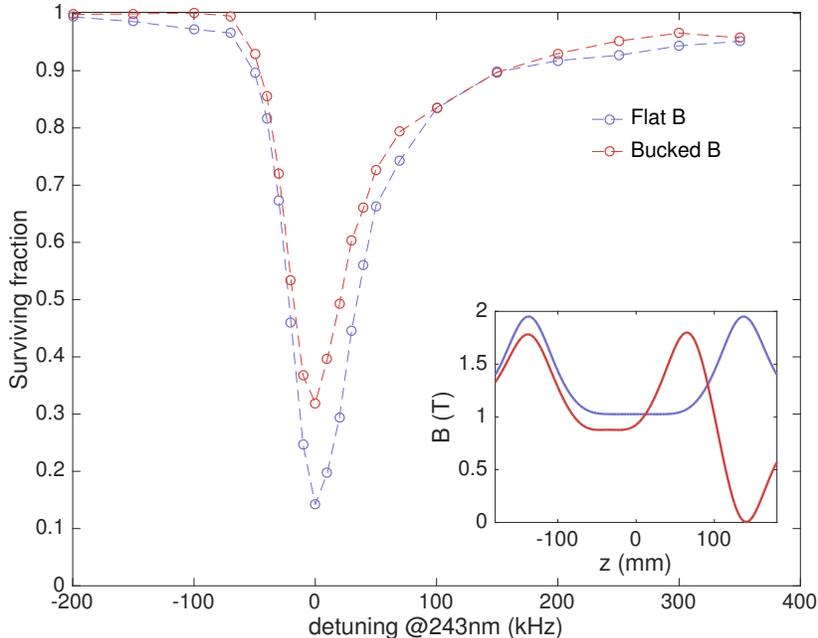
25

FIG. 7. Fraction of atoms which survive the simulated laser exposure in two different magnetic field configurations. For both fields configurations, an illumination of 250 s is simulated for each transition using 2 W of circulating laser power. The inset shows the on-axis magnetic field of in the two cases, and illustrates the local cancellation of the background field achieved with the "bucked" configuration.

357 tons pushed into this region to annihilate on the walls within the Silicon Vertex Detector. 358 The remaining 4 mirror coils can be used to produce the magnetic minimum trap, but as one 359 might expect, the uniformity of the magnetic well produced in this manner is less than what 360 can be achieved with all 5 mirror coils. In Figure 7, we investigate the effect of this change 361 in uniformity on the line shape. While the difference in survival rate in the two magnetic 362 field configurations is not big enough to exclude a measurement in either, there is a visible 363 benefit to using the more uniform field. This benefit can be understood as an increase in 364 the volume of the trap where the laser is on resonance with the transition.

365 **B. Line Shape**

366   In Figure 8, we plot the end states of simulations with different laser detunings, resulting 367 in the line shape for the chosen parameters. The response is slightly asymmetric with a

₃₆₈ tail extending to higher frequencies, which is a result of the remaining dependence of the
₃₆₉ transition frequency on the magnetic field strength. Since both transitions are shifted to
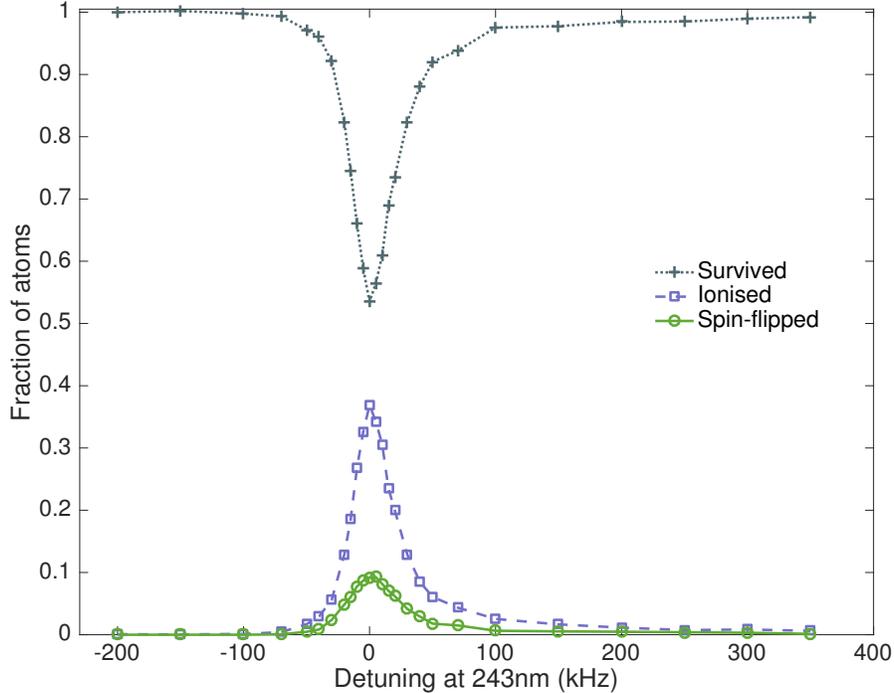₃₇₀ higher frequencies by higher magnetic fields, the tail is on the blue side of the peak.

FIG. 8. Fraction of simulated atoms respectively ionised, ejected through a spin-flip, and surviving
the full illumination time as a function of the detuning of the 243 nm laser. Assuming a flattened
₃₇₁ B-field, 1 W of laser power and 300 s illumination of each transition.

₃₇₂

₃₇₃   The FWHM of the peak in Figure 8 is just under 40 kHz and is dominated by the transit
₃₇₄ time broadening. In order to decrease this width for a more accurate determination of the
₃₇₅ center frequency, one can either reduce the speed of the atoms or increase the width of
₃₇₆ the laser beam, w_0. In Figure 9, we illustrate the latter through simulated lineshapes with
₃₇₇ different laser beam sizes. Decreasing the beam waist increases the laser intensity which
₃₇₈ increases both the excitation rate from $1S$ to $2S$ and the ionisation of $2S$ atoms. However,
₃₇₉ it also reduces the average time spent in the laser beam. As a first approximation, the
₃₈₀ transition rate scales as the laser intensity squared and therefore as w_0^{-4}. On the other
₃₈₁ hand, the volume occupied by the laser beam scales with w_0^2, so one would expect the
₃₈₂ transition rate to scale approximately as w_0^{-2}. The line shape is also expected to change
₃₈₃ with the beam waist. As long as the transition time broadening is the dominant broadening
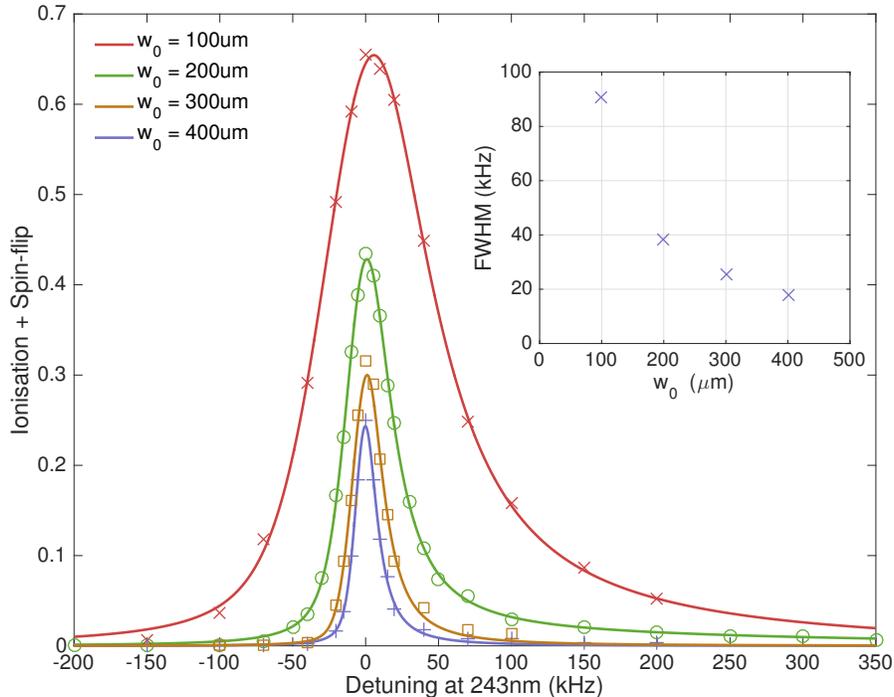
27

FIG. 9. Lineshapes simulated for different laser beam waists, w_0. The plotted signal is the fraction of atoms removed from the trap through either spin-flip or ionisation. For each beam waist, we simulate 300s exposures of each transition using $1\,\text{W}$ of laser power in our flattened field configuration. There is a trade-off between transition strength and line width: As the beam waist is made smaller the laser intensity increases and the transition time decreases, making the broadening more severe. Inset: The FWHM of the profiles derived from fits to an approximate functional shape.

mechanism, it follows from (40) that the width of the line should scale as w_0^{-1}. These simple geometric arguments of course ignore the details of the atomic orbits, but the predicted trends are reproduced in the full simulation results of Figure 9.

VII.   MEASUREMENT STRATEGIES

We have already mentioned a few ways in which excitations of $2S$ anti-atoms in a $1S$-$2S$ spectroscopy experiment might be detected. The disappearance mode detection as described earlier can be carried out in parallel with any scheme that results in a depletion of the number of trapped atoms left in the trap. Therefore, after further considering the merits of disappearance detection in the context of the current number of trapped antihydrogen

28

atoms in ALPHA as well as practical experimental constraints, we shall do the same for a number of schemes to provide an appearance signal.

In a disappearance measurement, which is by now an established technique in ALPHA [2, 16], the magnetic trap is shut down at the end of each experimental trial, allowing the number of remaining atoms to be counted. Since the detection happens only once per trial, the cosmic background contamination of this signal is typically orders of magnitude lower than the annihilation signal.

The downside lies in having to detect with statistical significance changes in the rate at which antihydrogen is still trapped at the end of an experimental trial. This requires a good null experiment with no depletion of the trapped population, performed in strict alternation with the measurement trials to avoid systematic effects stemming from changes in the rate at which antihydrogen is initially trapped. Additionally, the depletion of trapped atoms must be large, lest the number of trials needed to detect a difference from the null trials be too large. Specifically for our case, it is therefore favourable to drive out both the $|1S_c\rangle$ and the $|1S_d\rangle$ atoms, assumed to be trapped in equal amounts, by driving both the $1S_c - 2S_c$ and the $1S_d - 2S_d$ transitions. This was the strategy adopted for the first observation of the transition reported in Ref. [2]

A. Lyman-α Photons

As we noted in Section III, the $2S$ state of (anti)hydrogen can be made to decay to the $1S$ state essentially instantly by applying an electric field. As this rapid decay happens through the $2P$ states, a single photon is emitted with the full $1S$-$2S$ energy difference. Detecting this Lyman-α photon is the basis of detecting $1S$-$2S$ excitations in typical experiments with hydrogen [1, 18]. When not limited by solid angle, Lyman-α photons can be detected with high efficiency, and the difference in wavelength from the light needed to excite the transition enables good discrimination of stray $243\,\text{nm}$ photons stemming from the excitation laser or indeed from two-photon decays of the $2S$ atoms.

In experiments where antihydrogen is excited in a beam, the long lifetime of the metastable $2S$ state allows for complete separation of excitation and detection regions, which means a very good solid angle coverage for the Lyman-α detection can be achieved.

As described earlier, the ALPHA magnetic minimum trap is superimposed on the

Penning-Malmberg trap needed for producing cold antihydrogen. This severely limits the solid angle available for detecting photons from the trapped atoms which for ALPHA is about 10^{-5}. This exacerbates what is currently the primary constraint on antihydrogen experiments compared to ordinary hydrogen, which is the limited number of atoms available. Assuming laser parameters and trapped antihydrogen numbers like those realized in [2], the mean time between Lyman-α photon emissions is of order $\sim 10\,\mathrm{s}$. Combined with the constraints on solid angle, it seems currently unrealistic to have such a small number of photons provide a significant signal above background.

B. Spin-flip Ejection

In addition to the emission of a Lyman-α photon, making the $2S$ state decay through the mixing with $2P$ states allows for decays that change the hyperfine state. Some such decays will therefore result in a spin-flip, with the produced high field seeking atom being promptly ejected from the magnetic minimum trap and annihilating. These annihilations may be detected in ALPHA with $\sim 60\,\%$ efficiency, much better than what is allowed from solid angle considerations of Lyman-α photon detection in any minor modification to the current experimental setup.

An important parameter for the efficiency of using these annihilations as the detection method for $2S$ atoms is the fraction of electric field induced decays that result in a spin-flip, which we calculated for Figure 4 for both electric fields parallel to and perpendicular to the magnetic field.

While there is a maximum in this fraction of almost $70\,\%$, for an electric field parallel to a $\sim 0.1\,\mathrm{T}$ magnetic field, the spin-flips are much more rare at high magnetic fields. In the $\sim 1 - 2\,\mathrm{T}$ that trapped atoms can explore in ALPHA, about 10 excitations to the $2S$ state would be required to induce on average one spin-flip. With only one or two atoms trapped at a time, the signal from this process is then probably too low to feasibly distinguish from the background. However, with recent improvements in the number of atoms trapped, and in particular if further such improvements can be made, spin-flips could be a viable detection channel. Note however, that photoionisation is a competing channel through which atoms will leave the 2S state, thus deducting from the number of spin-flips produced. This is discussed further below.

C. Microwave Transition

The low efficiency in inducing spin-flips in simple electric field induced decays of the $2S$ state can be circumvented by resonantly driving the $2S$ population into a single $2P$ state, chosen to have a high probability to decay to an untrapped ground state. The ideal state to populate would have a very high probability of decaying to untrapped states, a non-zero electric dipole moment to $|2S_\alpha\rangle$, so the transition can be easily driven, and a transition frequency which does not overlap with any other transitions that would unintentionally depopulate either the $1S$ or the $2S$ states. Additionally, it would be convenient if the microwave radiation needed to drive the transition could be delivered without significant changes to the apparatus. Currently microwaves are delivered into the ALPHA electrode stack through a waveguide, which supports frequencies from $22\,\text{GHz}$ up to approximately $30\,\text{GHz}$, so we'll search for a transition frequency in this band.

In Figure 3, we plotted the energies of all the states in the $N = 2$ manifold. While $|2P_d\rangle$ has a $100\,\%$ chance of decaying to an untrapped ground state, there is no dipole moment to $|2S_\alpha\rangle$. The chance of spin-flips from $|2P_f\rangle$ is quite high ($\sim 85\,\%$ at 1T), and there is an electric dipole transition from $|2S_\alpha\rangle$. Unfortunately, the transition to $|2P_a\rangle$ has nearly the same frequency. In fact the two transition frequencies cross at almost exactly $B = 1\,\text{T}$, with $\text{f}(|2S_\alpha\rangle \rightarrow |2P_f\rangle)$ being larger for $B > 1\,\text{T}$ and both frequencies increasing with B. $|2P_a\rangle$ never decays to an untrappable ground state, so driving $|2S_\alpha\rangle \rightarrow |2P_a\rangle$ needs to be avoided. This can be done by lowering the bottom of the magnetic well below the crossing point of $1\,\text{T}$ and tuning the microwave radiation to be resonant with the $|2S_\alpha\rangle \rightarrow |2P_f\rangle$ transition at this field. This way, no magnetic field explorable by the trapped atoms brings $|2S_\alpha\rangle \rightarrow |2P_a\rangle$ into resonance.

In Figure 10 we plot the transition rates of these to microwave transitions as functions of magnetic field for two potential driving frequencies. The two peaks overlap at $\sim 1\,\text{T}$ for a drive frequency of $\sim 24\,\text{GHz}$. Notice that for both the plotted microwave frequencies, the $|2P_f\rangle$ peak is sitting on the tail of the $|2P_a\rangle$ peak, meaning some fraction of atoms will be driven to the $|2P_a\rangle$ state, lowering the efficiency of flipping the spins a bit. In the $22.5\,\text{GHz}$ case, around $\sim 80\,\%$ of the atoms that are driven to a 2P state by the microwave radiation, decay to an untrapped atom.

Having established that a large fraction of atoms excited to the $2S$ state can be brought
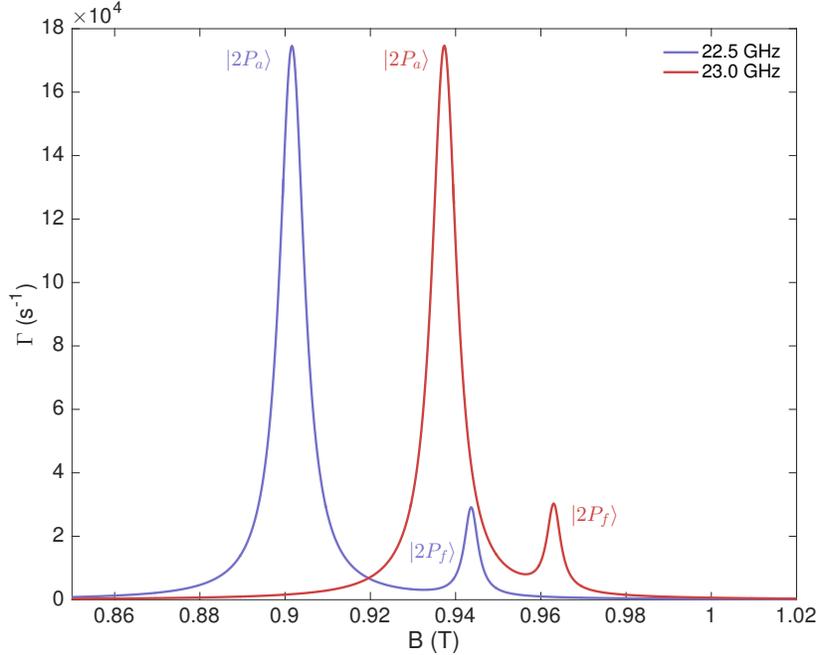
FIG. 10. Microwave transition rates out of the low field seeking $2S$ states, calculated for two different frequencies as functions of magnetic field. Assumes $1\,\mathrm{mW/cm^2}$ of microwave intensity. The peaks due to transitions to the $|2P_a\rangle$ and $|2P_f\rangle$ are labeled. The electric dipole moment to $|2P_a\rangle$ is much larger than to $|2P_f\rangle$ and in particular in the $23\,\mathrm{GHz}$ case, the $|2P_f\rangle$ peak is sitting on the tail of the $|2P_a\rangle$ peak, making it difficult to drive only the one transition.

to annihilate to produce signal in the detector, we consider how to optimise the ratio of the expected signal to the background rate of cosmic events in the annihilation detector. By pulsing the microwave radiation and only looking for annihilation events during the pulse, the number of integrated background events can be reduced drastically. Of course, the signal is also reduced, as atoms can potentially decay out of the $2S$ state before a microwave pulse is turned on to drive them into a $2P$ state. Clearly, for this to be an efficient detection method, the time between microwave pulses should not be longer than the mean lifetime of $2S$ atoms in the trap, which we estimated above to be reduced from the natural lifetime of $122\,\mathrm{ms}$ to around $50\,\mathrm{ms}$ by the motional electric field. The other parameter that could potentially be tuned is the length of the microwave pulse applied. The shorter time needed to drive the microwave transition, the shorter the detection window can be. There is a however a lower limit on the length of detection window, set by the trapped atom dynamics: Once the spin of an antihydrogen atom has been flipped, it still has to travel to the wall of the apparatus

before it annihilates. A good estimate for how long this can take is the radial bounce time for the trapped atoms, which is $\sim 1\,\mathrm{ms}$. These considerations of pulsed detection also apply directly to detection through (DC) electric field induced decays with spin-flips, as well as for the detection of Lyman-α photons, although with a different background rate for whichever single photon detector is considered.

We conclude that a resonant microwave transition can provide an improvement in the efficiency of detecting rare 1S-2S excitations, compared to inducing decays with a DC electric field, and is realizable without any significant changes to the ALPHA apparatus. The cost of this improvement is the need to drive both an optical and a microwave transition to produce the signal.

D. Photo-Ionisation

Finally we turn our attention to potentially exploiting that a single $243\,\mathrm{nm}$ photon can ionise the $2S$ state in (anti)hydrogen. Detecting the produced ions has been suggested for a range of two-photon spectroscopy experiments, where one additional photon from the exciting laser beam photo-ionises the excited state [20]. This is an effect that we have until now left out of the discussions of the detection methods above, but which affects them all, since photo-ionisation is a competing mechanism for leaving the $2S$ state. Especially at the high powers needed to excite the very small numbers of currently trapped antihydrogen atoms, photo-ionisation is quite significant as evidenced by Figure 6.

A potential advantage of using photo-ionisation as the detection method is that the antiprotons produced by photo-ionisation may be stored for much longer than the lifetime of the $2S$ in the atom, which limits the achievable SNR in all of the above schemes. Since by design the entire volume accessible to trapped atoms in ALPHA is surrounded by Penning trap electrodes, the antiprotons produced by photo-ionising antihydrogen can in principle be contained. Furthermore, the energy of the antiprotons created will be similar to that of the trapped atoms, meaning small electric potentials are sufficient to confine them. This means that the perturbing effect on the nearby trapped antihydrogen can be kept negligible.

In order to detect the antiprotons created from photo-ionisation, they could e.g. be ejected onto a MicroChannel Plate (MCP). In ALPHA, an MCP and phosphorous plate assembly located on the axis of the Penning trap and about $2\,\mathrm{m}$ away from the center of the

33

magnetic minimum trap, is already used to measure the radial density profile of plasmas in the Penning-Malmberg trap [26]. Plasmas in ALPHA are typically $< 1\,\mathrm{mm}$ in radius and the current MCP setup measures particles coming from up to around $r = 1\,\mathrm{mm}$, which is much smaller than the space explored by trapped neutral atoms. However, due to the small angle between the Penning trap axis and the laser beam, most of the photo-ionisations happen at sufficiently small radii to be measurable by the MCP without changes to the setup or field geometry.

As photo-ionisation is intrinsic to the measurement at the laser-powers sufficient to achieve a detectable disappearance signal a "test" of this "scheme" was automatically carried out in the recent observation of the $1S$-$2S$ transition [2]. As it turned out the antiprotons resulting from photo-ionisation were not well contained by the neutral atom trapping fields as they were all lost and annihilated during the laser-illumination. This is not inconsistent with previous experiments observing deterioration of trap lifetimes in long wells in inhomogeneous magnetic fields [e.g. Ref. [27]]. Caveat methods to counter this issue, appearance measurements will be limited by the background stemming from the long laser exposure times. Increased laser-power would reduce the necessary exposure time, but would also result in increased broadening, something that one eventually would like to avoid.

E. Bucked Magnetic Field

Another option for detecting the photo-ionised atoms, which we have already briefly mentioned, relies on the antimatter nature of the produced antiprotons. If the antiprotons are brought to annihilate within the silicon vertex detector, they can be detected with the well known efficiency and cosmic background rejection of this detector. In our most traditional magnetic field configurations, the external solenoid ensures that all field lines which are close to the axis extend far beyond the Penning trap electrodes and the annihilation detector, preventing charged particles from moving radially and annihilating on the walls - this is indeed part of the operating principle of a Penning trap. However, by cancelling the field from the external solenoid with an equal and opposite field provided by one of our mirror coils, all field lines are forced into the walls in a small region around the field-cancelling or bucking coil, providing a path for the charged antiprotons to annihilate.

Naturally, using one of the mirror coils for cancelling the field in one region of the trap

leaves both a smaller region in which to keep antihydrogen trapped and fewer coils with which to make the bottom of the trap as uniform as possible. The effect of this is seen in Figure 7, where we plotted results of simulations which are identical apart from the choice of magnetic field. This decrease in excitation rate obviously limits the appeal of this technique for detecting the $2S$ atoms. Furthermore, in light of the observed short lifetime of antiprotons in the current trap configuration discussed in the previous section this additional method for ejecting particles has no obvious added value for the time being and will not be discussed further.

F.   Measuring the line shape

Having discussed the various strategies above, ALPHA settled on using disappearance as the primary measurement tool for its recent observation of the $1S$-$2S$ transition [2] and due to the short lifetime of antiprotons from photo ionisation exploited the low detector background analysis to detect annihilations in the 600 s laser-illumination periods as supporting evidence. The difficulty, as exemplified by the published data, is that one is either looking for a (potentially) small reduction in a low rate signal (disappearance) or for a small signal on a relatively large background (appearance). Which is most appropriate will have to be evaluated on a case-by-case basis. In order to measure the line shape, several different laser detunings will be necessary, each with a different degree of ejection of trapped anti-atoms. Without elaborating on all the possible scenarios, let us assume that one may be able to reproduce measurements of the type in Ref. [2] with, say five different detunings bracketing the line centre. Relying on disappearance alone and requiring similar statistical significance for each point as in Ref. [2], we'll need about an order of magnitude more trials, as it becomes increasingly hard to distinguish smaller fractional disappearance. This is a realistic scenario as it uses a similar number of trials to what was done in the spin-flip experiment [16]. The resulting data should allow determination of the line-centre of the ~40kHz wide line (FWHM) to within ~10 kHz, or a relative precision of ~10^{-11}. Further refinement of the experiment, in particular higher trapping rates achieved either through colder antihydrogen or further antihydrogen stacking should allow the current experimental setup to eventually reach the limit of the calculations in this paper.

VIII.   SUMMARY AND OUTLOOK

We have presented calculations and simulations pertaining to $1S$-$2S$ spectroscopy of magnetically trapped antihydrogen atoms. Part of this work guided the experimental choices that led to the first observation of the $1S$-$2S$ transition in antihydrogen [2]. We focused on the challenges of measuring on the few antihydrogen atoms that may be trapped compared to the copious amounts of hydrogen one may interrogate either trapped or in beams. In particular we find that detection is currently limited to methods that result in the controlled annihilation of the antihydrogen atom (or more specifically the antiproton), and even then that it is currently not advantageous to rely solely on a spin-flip of the anti-atom in order to eject it from the trap, rather it must be photo-ionised. While photo-ionisation relies on significant laser-power and eventually results in measurable broadening, the current main limitation on line-width, and hence precision of the measurement is the transit-time induced broadening due to the temperature of the trapped antihydrogen. Transit time broadening currently dominates the line width with realistic ALPHA parameters. An overview of the broadening effects we have considered is given in Table II. With either significant cooling (e.g. laser-cooling [24]), or a step increase in the number of antihydrogen atoms that would allow throwing away the hot ones [28] as well increasing the laser beam size, this may eventually be reduced to approach the limit of the calculations in this paper. We are looking forward to the first measurements of the line shape of the $1S$-$2S$ in trapped antihydrogen that we expect will give a line-centre measurement precision in the 10^{-11} range and thus result in the lowest energy CPT test yet to be accomplished on antimatter [29, 30].

[1] C. G. Parthey, A. Matveev, J. Alnis, B. Bernhardt, A. Beyer, R. Holzwarth, A. Maistrou, R. Pohl, K. Predehl, T. Udem, T. Wilken, N. Kolachevsky, M. Abgrall, D. Rovera, C. Salomon, P. Laurent, and T. W. Hänsch, Phys. Rev. Lett. **107**, 203001 (2011).

[2] M. Ahmadi, B. X. R. Alves, C. J. Baker, W. Bertsche, E. Butler, A. Capra, C. Carruth, C. L. Cesar, M. Charlton, S. Cohen, R. Collister, S. Eriksson, A. Evans, N. Evetts, J. Fajans,

T. Friesen, M. C. Fujiwara, D. R. Gill, A. Gutierrez, J. S. Hangst, W. N. Hardy, M. E. Hayden, C. A. Isaac, A. Ishida, M. A. Johnson, S. A. Jones, S. Jonsell, L. Kurchaninov, N. Madsen, M. Mathers, D. Maxwell, J. T. K. McKenna, S. Menary, J. M. Michan, T. Momose, J. J. Munich, P. Nolan, K. Olchanski, A. Olin, P. Pusa, C. Ø. Rasmussen, F. Robicheaux, R. L. Sacramento, M. Sameed, E. Sarid, D. M. Silveira, S. Stracka, G. Stutter, C. So, T. D. Tharp, J. E. Thompson, R. I. Thompson, D. P. van der Werf, and J. S. Wurtele, Nature **541**, 506 (2017).

[3] G. B. Andresen, M. D. Ashkezari, M. Baquero-Ruiz, W. Bertsche, P. D. Bowe, E. Butler, C. L. Cesar, S. Chapman, M. Charlton, A. Deller, S. Eriksson, J. Fajans, T. Friesen, M. C. Fujiwara, D. R. Gill, A. Gutierrez, J. S. Hangst, W. N. Hardy, M. E. Hayden, A. J. Humphries, R. Hydomako, M. J. Jenkins, S. Jonsell, L. V. Jørgensen, L. Kurchaninov, N. Madsen, S. Menary, P. Nolan, K. Olchanski, A. Olin, A. Povilus, P. Pusa, F. Robicheaux, E. Sarid, S. S. E. Nasr, D. M. Silveira, C. So, J. W. Storey, R. I. Thompson, D. P. van der Werf, J. S. Wurtele, and Y. Yamazaki, Nature (London) **468**, 673 (2010).

[4] G. Gabrielse, R. Kalra, W. S. Kolthammer, R. McConnell, P. Richerme, D. Grzonka, W. Oelert, T. Sefzick, M. Zielinski, D. W. Fitzakerley, M. C. George, E. A. Hessels, C. H. Storry, M. Weel, A. Müllers, and J. Walz, Phys. Rev. Lett. **108**, 113002 (2012).

[5] W. A. Bertsche, E. Butler, M. Charlton, and N. Madsen, Journal of Physics B: Atomic, Molecular and Optical Physics **48**, 232001 (2015).

[6] J. H. Malmberg and C. F. Driscoll, Phys. Rev. Lett. **44**, 654 (1980).

[7] T. M. ONeil, The Physics of Fluids **23**, 2216 (1980).

[8] S. Maury, Hyperfine Interactions **109**, 43 (1997).

[9] C. Amole, G. Andresen, M. Ashkezari, M. Baquero-Ruiz, W. Bertsche, P. Bowe, E. Butler, A. Capra, P. Carpenter, C. Cesar, S. Chapman, M. Charlton, A. Deller, S. Eriksson, J. Escallier, J. Fajans, T. Friesen, M. Fujiwara, D. Gill, A. Gutierrez, J. Hangst, W. Hardy, R. Hayano, M. Hayden, A. Humphries, J. Hurt, R. Hydomako, C. Isaac, M. Jenkins, S. Jonsell, L. Jørgensen, S. Kerrigan, L. Kurchaninov, N. Madsen, A. Marone, J. McKenna, S. Menary, P. Nolan, K. Olchanski, A. Olin, B. Parker, A. Povilus, P. Pusa, F. Robicheaux, E. Sarid, D. Seddon, S. S. E. Nasr, D. Silveira, C. So, J. Storey, R. Thompson, J. Thornhill, D. Wells, D. van der Werf, J. Wurtele, and Y. Yamazaki, Nuclear Instruments and Methods in Physics Research Section A: Accelerators, Spectrometers, Detectors and Associated Equipment **735**,

37

646 319 (2014).

647 [10] W. Bertsche, A. Boston, P. D. Bowe, C. L. Cesar, S. Chapman, M. Charlton, M. Chartier,
648 A. Deutsch, J. Fajans, M. C. Fujiwara, R. Funakoshi, K. Gomberoff, J. S. Hangst, R. S.
649 Hayano, M. J. Jenkins, L. V. Jørgensen, P. Ko, N. Madsen, P. Nolan, R. D. Page, L. G. C.
650 Posada, A. Povilus, E. Sarid, D. M. Silveira, D. P. van der Werf, Y. Yamazaki, B. Parker,
651 J. Escallier, and A. Ghosh, Nuclear Instruments and Methods in Physics Research A **566**,
652 746 (2006).

653 [11] G. B. Andresen, M. D. Ashkezari, M. Baquero-Ruiz, W. Bertsche, P. D. Bowe, E. Butler,
654 C. L. Cesar, M. Charlton, A. Deller, S. Eriksson, J. Fajans, T. Friesen, M. C. Fujiwara, D. R.
655 Gill, A. Gutierrez, J. S. Hangst, W. N. Hardy, R. S. Hayano, M. E. Hayden, A. J. Humphries,
656 R. Hydomako, S. Jonsell, S. L. Kemp, L. Kurchaninov, N. Madsen, S. Menary, P. Nolan,
657 K. Olchanski, A. Olin, P. Pusa, C. Ø. Rasmussen, F. Robicheaux, E. Sarid, D. M. Silveira,
658 C. So, J. W. Storey, R. I. Thompson, D. P. van der Werf, J. S. Wurtele, and Y. Yamazaki,
659 Nat Phys **7**, 558 (2011).

660 [12] G. B. Andresen, M. D. Ashkezari, M. Baquero-Ruiz, W. Bertsche, P. D. Bowe, E. Butler,
661 C. L. Cesar, S. Chapman, M. Charlton, A. Deller, S. Eriksson, J. Fajans, T. Friesen, M. C.
662 Fujiwara, D. R. Gill, A. Gutierrez, J. S. Hangst, W. N. Hardy, M. E. Hayden, A. J. Humphries,
663 R. Hydomako, M. J. Jenkins, S. Jonsell, L. V. JØrgensen, L. Kurchaninov, N. Madsen, J. T. K.
664 McKenna, S. Menary, P. Nolan, K. Olchanski, A. Olin, A. Povilus, P. Pusa, F. Robicheaux,
665 J. Sampson, E. Sarid, D. Seddon, S. S. el Nasr, D. M. Silveira, C. So, J. W. Storey, R. I.
666 Thompson, J. Thornhill, D. Wells, D. P. van der Werf, J. S. Wurtele, and Y. Yamazaki,
667 Journal of Instrumentation **7**, C01051 (2012).

668 [13] G. Andresen, M. Ashkezari, W. Bertsche, P. Bowe, E. Butler, C. Cesar, S. Chapman, M. Charl-
669 ton, A. Deller, S. Eriksson, J. Fajans, T. Friesen, M. Fujiwara, D. Gill, A. Gutierrez, J. Hangst,
670 W. Hardy, M. Hayden, R. Hayano, A. Humphries, R. Hydomako, S. Jonsell, L. Jørgensen,
671 L. Kurchaninov, N. Madsen, S. Menary, P. Nolan, K. Olchanski, A. Olin, A. Povilus, P. Pusa,
672 E. Sarid, S. S. el Nasr, D. Silveira, C. So, J. Storey, R. Thompson, D. van der Werf, and
673 Y. Yamazaki, Nuclear Instruments and Methods in Physics Research Section A: Accelerators,
674 Spectrometers, Detectors and Associated Equipment **684**, 73 (2012).

675 [14] C. Amole, G. B. Andresen, M. D. Ashkezari, M. Baquero-Ruiz, W. Bertsche, E. Butler,
676 C. L. Cesar, S. Chapman, M. Charlton, A. Deller, S. Eriksson, J. Fajans, T. Friesen, M. C.

38

Fujiwara, D. R. Gill, A. Gutierrez, J. S. Hangst, W. N. Hardy, M. E. Hayden, A. J. Humphries, R. Hydomako, L. Kurchaninov, S. Jonsell, N. Madsen, S. Menary, P. Nolan, K. Olchanski, A. Olin, A. Povilus, P. Pusa, F. Robicheaux, E. Sarid, D. M. Silveira, C. So, J. W. Storey, R. I. Thompson, D. P. van der Werf, and J. S. Wurtele, New Journal of Physics **14**, 015010 (2012).

[15] Alpha Collaboration, G. B. Andresen, W. Bertsche, P. D. Bowe, C. Bray, E. Butler, C. L. Cesar, S. Chapman, M. Charlton, J. Fajans, M. C. Fujiwara, D. R. Gill, J. S. Hangst, W. N. Hardy, R. S. Hayano, M. E. Hayden, A. J. Humphries, R. Hydomako, L. V. Jørgensen, S. J. Kerrigan, L. Kurchaninov, R. Lambo, N. Madsen, P. Nolan, K. Olchanski, A. Olin, A. Povilus, P. Pusa, F. Robicheaux, E. Sarid, S. S. El Nasr, D. M. Silveira, J. W. Storey, R. I. Thompson, D. P. van der Werf, J. S. Wurtele, and Y. Yamazaki, Physics Letters B **685**, 141 (2010).

[16] C. Amole, M. D. Ashkezari, M. Baquero-Ruiz, W. Bertsche, P. D. Bowe, E. Butler, A. Capra, C. L. Cesar, M. Charlton, A. Deller, P. H. Donnan, S. Eriksson, J. Fajans, T. Friesen, M. C. Fujiwara, D. R. Gill, A. Gutierrez, J. S. Hangst, W. N. Hardy, M. E. Hayden, A. J. Humphries, C. A. Isaac, S. Jonsell, L. Kurchaninov, A. Little, N. Madsen, J. T. K. McKenna, S. Menary, S. C. Napoli, P. Nolan, K. Olchanski, A. Olin, P. Pusa, C. O. Rasmussen, F. Robicheaux, E. Sarid, C. R. Shields, D. M. Silveira, S. Stracka, C. So, R. I. Thompson, D. P. van der Werf, and J. S. Wurtele, Nature **483**, 439 (2012).

[17] Bethe, H. A. and Salpeter, E. E., *Quantum Mechanics of One- and Two-Electron Atoms*, 1st ed. (Springer, 1957).

[18] C. L. Cesar, D. G. Fried, T. C. Killian, A. D. Polcyn, J. C. Sandberg, I. A. Yu, T. J. Greytak, D. Kleppner, and J. M. Doyle, Phys. Rev. Lett. **77**, 255 (1996).

[19] J. T. M. Walraven and I. F. Silvera, Review of Scientific Instruments **53**, 1167 (1982).

[20] M. Haas, U. D. Jentschura, C. H. Keitel, N. Kolachevsky, M. Herrmann, P. Fendel, M. Fischer, T. Udem, R. Holzwarth, T. W. Hänsch, M. O. Scully, and G. S. Agarwal, Phys. Rev. A **73**, 052501 (2006).

[21] E. Forest and R. D. Ruth, Phys. D **43**, 105 (1990).

[22] H. Yoshida, Physics Letters A **150**, 262 (1990).

[23] J. Candy and W. Rozmus, Journal of Computational Physics **92**, 230 (1991).

[24] P. H. Donnan, M. C. Fujiwara, and F. Robicheaux, Journal of Physics B: Atomic, Molecular and Optical Physics **46**, 025302 (2013).

[25] C. Amole, M. D. Ashkezari, M. Baquero-Ruiz, W. Bertsche, E. Butler, A. Capra, C. L. Cesar, M. Charlton, S. Eriksson, J. Fajans, T. Friesen, M. C. Fujiwara, D. R. Gill, A. Gutierrez, J. S. Hangst, W. N. Hardy, M. E. Hayden, C. A. Isaac, S. Jonsell, L. Kurchaninov, A. Little, N. Madsen, J. T. K. McKenna, S. Menary, S. C. Napoli, P. Nolan, A. Olin, P. Pusa, C. Ø. Rasmussen, F. Robicheaux, E. Sarid, D. M. Silveira, C. So, R. I. Thompson, D. P. van der Werf, J. S. Wurtele, A. Zhmoginov, and A. E. Charman, Nat Commun **4**, 1785 (2013), supplementary information available for this article at http://www.nature.com/ncomms/journal/v4/n4/suppinfo/ncomms2787_S1.html.

[26] G. B. Andresen, W. Bertsche, P. D. Bowe, C. C. Bray, E. Butler, C. L. Cesar, S. Chapman, M. Charlton, J. Fajans, M. C. Fujiwara, D. R. Gill, J. S. Hangst, W. N. Hardy, R. S. Hayano, M. E. Hayden, A. J. Humphries, R. Hydomako, L. V. Jørgensen, S. J. Kerrigan, L. Kurchaninov, R. Lambo, N. Madsen, P. Nolan, K. Olchanski, A. Olin, A. P. Povilus, P. Pusa, E. Sarid, S. S. El Nasr, D. M. Silveira, J. W. Storey, R. I. Thompson, D. P. van der Werf, and Y. Yamazaki, Review of Scientific Instruments **80**, 123701 (2009).

[27] J. Notte and J. Fajans, Physics of Plasmas **1**, 1123 (1994), http://dx.doi.org/10.1063/1.870762.

[28] N. Madsen, F. Robicheaux, and S. Jonsell, New Journal of Physics **16**, 063046 (2014).

[29] R. BLUHM, "Probing the planck scale in low-energy atomic physics," in *CPT and Lorentz Symmetry* (WORLD SCIENTIFIC, 2011) pp. 16–25.

[30] V. A. Kostelecký and A. J. Vargas, Phys. Rev. D **92**, 056002 (2015).